

Review

Interfacial Tuning of Polymeric Composite Materials for High-Performance Energy Devices

Balaraman Vedhanarayanan ^{1,*},[†] , K. C. Seetha Lakshmi ^{2,*},[†]  and Tsung-Wu Lin ^{3,*}¹ Department of Applied Chemistry and Biotechnology, Graduate School of Engineering, Chiba University, 1-33 Yayoi-cho, Inage-ku, Chiba 263-8522, Japan² Department of Chemistry, Graduate School of Science, Chiba University, 1-33 Yayoi-cho, Inage-ku, Chiba 263-8522, Japan³ Department of Chemistry, Tunghai University, No. 1727, Section 4, Taiwan Boulevard, Xitun District, Taichung City 407, Taiwan

* Correspondence: bvedhanarayanan@gmail.com (B.V.); seethakc@gmail.com (K.C.S.L.); twlin@thu.edu.tw (T.-W.L.)

† These authors contributed equally to this work.

Abstract: Polymeric composite materials attracted attention when pristine polymers alone could not fulfill the necessity of high-performance functional materials for wide applications. Mixing two or more polymers (blends) together or compositing the polymers with inorganic compounds/carbon-based nanomaterials greatly solved the problem associated with the mechanical, thermal, and electronic properties along with the chemical stability, which paves a new pathway for optimizing the functional properties of active materials. However, a mere mixing of individual components sometimes would not provide enhanced properties due to the formation of phase-separated, larger domains of components. In particular, the grain boundaries of components, also known as “interfaces”, actually determine the properties of these composite materials. The tuning of interfacial properties is significant to achieve composites with higher electrical conductivity and better charge transfer kinetics if they are targeted toward high-performance energy devices. This review aims to provide an overview of recent advancements in the area of polymeric composite materials with tuned interfacial characteristics towards energy conversion (solar cells, photocatalytic hydrogen production, and nanogenerators) and energy storage (supercapacitors and metal-ion batteries) devices with very recent representative examples.

Keywords: polymer composites; interfacial properties; solar cells; photocatalytic hydrogen production; supercapacitors; batteries; polymeric composite electrolytes



Citation: Vedhanarayanan, B.; Lakshmi, K.C.S.; Lin, T.-W. Interfacial Tuning of Polymeric Composite Materials for High-Performance Energy Devices. *Batteries* **2023**, *9*, 487. <https://doi.org/10.3390/batteries9100487>

Academic Editors: Carlos Ziebert and Ivana Hasa

Received: 24 June 2023

Revised: 21 August 2023

Accepted: 20 September 2023

Published: 25 September 2023



Copyright: © 2023 by the authors. Licensee MDPI, Basel, Switzerland. This article is an open access article distributed under the terms and conditions of the Creative Commons Attribution (CC BY) license (<https://creativecommons.org/licenses/by/4.0/>).

1. Introduction

Effective utilization of renewable energy resources and minimization of conventional fossil fuels can address the problems associated with energy scarcity and climate change [1,2]. The development of sustainable energy harvesting and storage systems is necessary to fulfill our present and future energy demands [3]. Renewable energy sources include solar, wind, thermal, mechanical, and biomass [4,5]. The major energy harvesting devices such as photovoltaics, photoelectrochemical cells, and energy nanogenerators convert the available forms of energy (sunlight, heat, vibration, stress, and friction) into electricity. Solar energy is an important form of renewable energy. Earth receives more than 3 million exajoules of energy (1 exajoule equals to 10^{18} J) every year [6]. In the vast amount of energy, less than 0.1% is used by plants for biomass production. These data imply that we have plenty more energy than we exactly require for our use in a year. However, the lack of efficient energy harvesting and storage systems is a primary reason for our energy crisis. The development of photovoltaic (solar cells; SoC) and photoelectrochemical devices has satisfied a certain percentage of energy demand in a sustainable manner [7].

Among the various types of solar cells, silicon (Si-SoC), dye-sensitized (DSSC) [8], Perovskite [9], and bulk-heterojunction polymer (BHJ) [10] solar cells are the most widely exploited photovoltaic devices. The highest power conversion efficiency (PCE) of a single Si-SC is only ~25% (GaAs thin film-based devices can achieve up to 28%), and the other DSSC and BHJ usually exhibit a lower PCE than that of Si or GaAs-based devices. Though the PCE of BHJ devices is relatively low, they are highly preferred due to their low cost, easy processability, flexibility, and lightweight nature compared to Si-SoCs. On the other hand, photoelectrochemical devices [11] convert solar energy into storable and portable chemical energy, such as hydrogen, by splitting water [12,13]. Hydrogen is a primary component in fuel cells that transform chemical energy (hydrogen) into electricity with zero carbon emissions, as it has a specific energy of 142 MJ kg^{-1} (the highest of currently available fuels) [14]. In addition to solar energy, other forms of available energy such as thermal, mechanical vibration/stress, and friction can also be converted into electricity by using energy nanogenerators, namely, thermoelectric [15], piezoelectric [16] and triboelectric [17] devices. The efficiency of these energy harvesting devices is mainly dependent on material properties and device structures.

Energy storage devices play a crucial role in renewable energy management, as the energy harvested from sustainable resources should be efficiently stored and supplied when required. Electrochemical capacitors, or supercapacitors [18] and rechargeable batteries [19] are the primary energy storage devices that are widely employed for this purpose. Supercapacitors are capacitors with a better ability to store more power. They can store and deliver energy at a faster rate in a larger number of repeated cycles than rechargeable batteries. However, supercapacitors are capable of storing only a lower energy density and possess a low breakdown voltage when compared to batteries. These energy storage devices are usually fabricated with various structures and a range of storage capacities based on the requirements. For example, if an energy storage device is used for wearable health monitoring sensors, the device structure should be more flexible and lightweight [20].

The evolution of nanomaterials has revolutionized energy harvesting and storage devices to a greater extent for diverse applications. Currently, varieties of nanomaterials based on inorganic semiconductors [21], metal nanoparticles [22], ceramics [23], metal compounds [24], organic functional molecules [25], and polymers [26] have been developed as active materials in these energy devices [27]. The performance of the active material is further improved by combining two or more individual components with better interfacial properties such as surface adhesion, domain morphology, distribution of heterojunctions, interdiffusion, and charge-transfer kinetics. All these properties could effectively be controlled by the proper introduction of molecular-level interactions (noncovalent as well as covalent bonding) among the different components of the polymeric composite materials. In this review, the various types of polymer-based composite materials and their energy harvesting as well as energy storage characteristics in terms of interfacial characteristics (Figure 1) are discussed under different sections with very recent representative examples. Section 2 elaborates on the role of polymer-composite materials in significant energy conversion devices such as solar cells, photocatalytic hydrogen generation, thermoelectric, piezoelectric, and triboelectric nanogenerators. Further, the high-performance polymer-composite-based materials, which act as electrodes, solid electrolytes, binders, and separators, are described in Section 3 for energy storage devices such as supercapacitors and metal-ion batteries. Finally, the future perspectives of these composite materials for advanced energy devices are detailed in Section 4.

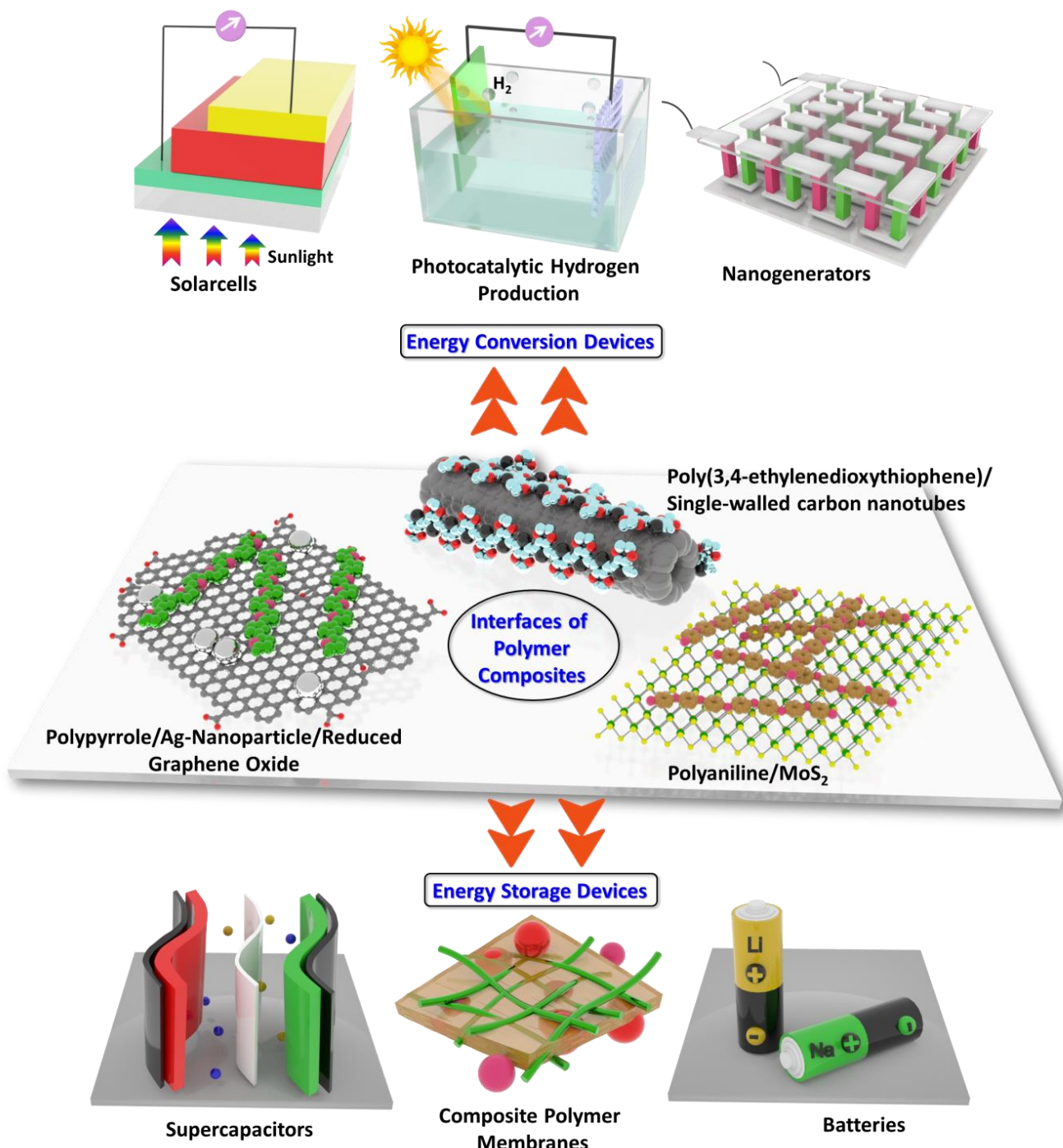


Figure 1. A schematic representation shows the various polymer composites and their energy applications. As representative examples, the composites of poly(3,4-ethylenedioxythiophene)/single-walled carbon nanotubes, polypyrrole/silver (Ag) nanoparticles/reduced graphene oxide (rGO), and polyaniline/molybdenum disulfide (MoS₂) and their various energy conversion (solar cells, hydrogen production, and nanogenerators) and storage (supercapacitors, composite polymer membranes, and batteries) devices are shown here.

2. Interfaces of Energy Harvesting Materials

2.1. Solar Cells

Solar cells made up of semiconducting polymers and inorganic nanomaterials are considered potential energy harvesting devices that could achieve an impressive power conversion efficiency (PCE—defined as the percentage of the total power of the incident

light radiation that is converted into electricity), which cannot be achieved by the cells with either polymer or inorganic counterparts [28]. Though polymer solar cells have opened a new pathway towards flexible energy harvesting devices when compared to the heavy and fragile conventional silicon solar cells, the low charge carrier mobility that limits their PCE is a major disadvantage [29]. It could be overcome by compositing with topologically tuned inorganic materials or carbon nanomaterials such as carbon nanotubes/fullerene derivatives [30]. Several semiconducting polymers are broadly used in polymer-based solar cells, which include poly(3-hexylthiophene) (P3HT), poly(2-methoxy-5-(2-ethylhexyloxy)-1,4-phenylenevinylene) (MEH-PPV), and poly((9,9-diptyfluorene)-2,7-diyl-alt-(4,7-bis(3-hexylthien-5-yl)-2,1,3-benzothiadiazole)-2',2''-diyl) (F8TBT) [31]. Here, the polymer acts as a donor, whereas the inorganic components serve the role of acceptor, which makes the pool of heterojunctions (interfaces) play an important role in the charge separation followed by their migration (Figure 2a) [31]. The PCE is mainly dependent on the nature and concentration of heterojunctions while mixing the solution-processing donor polymers with their acceptor counterparts. In this section, the exploitation of polymer-based composite materials in the field of energy harvesting devices is discussed in detail.

2.1.1. Semiconducting Polymers and Metal/Metal Oxides-Based Composites

The polymer composites of noble metal nanostructures play a crucial role in the fabrication of flexible solar cells. For instance, the composite of PEDOT:PSS (poly(3,4-ethylene dioxythiophene):polystyrene sulphone) and silver nanowire (Ag NW) is utilized as top electrodes over the active layer of solar cells, as the PEDOT:PSS/Ag NW composite has higher transparency [32]. The fabricated solar cell module with 10 sub-cells exhibited better flexibility and possessed a PCE of >12% (Table 1). The Ag-NW-based top electrode effectively reduces the leakage current and significantly improves the mechanical stability of the device. Similarly, in polymer/metal oxide composites, porous TiO_2 is the widely used transition metal oxide counterpart [33]. In general, the PCE and the external quantum efficiency (EQE—defined as the ratio of the number of charge carriers collected and the total number of incident photons) are the important parameters that measure the ability of solar cells to convert incident light energy into electricity. In the case of polymer/ TiO_2 structures, the nature of polymers, porosity of TiO_2 , and thickness of the composite layers determine the PCE and EQE of the devices. In addition, the structure of the device also plays a crucial role in achieving better efficiency. Fill factor (FF) is defined as the quantity of maximum power that can be achieved by the cell, and it is calculated by multiplying the open-circuit voltage and short-circuit current of that device [34]. In a typical hybrid solar cell, the acceptor metal oxide layer is usually deposited over the conducting indium-tin-oxide (ITO)-coated transparent glass substrate, and a thin metal layer coated over the active material acts as a hole-transporting medium to the external circuit. It is important to insulate the charge collector from the polymer material to avoid the charge leakage of the device, which ultimately leads to a lower fill factor [35]. Therefore, when a polymer/metal oxide active layer is used in a hybrid device, PEDOT:PSS (doped conducting polymer) is employed for the insulation of the donor polymer from the charge-collecting layer (Figure 2b) [36]. Another factor that determines the performance of the hybrid device is the work function of the anode (thin metal layer). The poor matching of the HOMO of the polymer and the work function of the anode usually results in low interfacial conductivity and an inferior fill factor. Proper selection of the anode can improve the overall performance of the hybrid solar cells.

Table 1. Selected list of polymer composite materials for energy conversion devices.

S.No.	Polymer Composites of Energy Conversion Devices					
	Material	Cell classification	Solar cells Open Circuit voltage (V)	Fill Factor	PCE	Ref.
1.	PEDOT:PSS/Ag NW (Module of 10 sub cells)	Multi-layer	8.35	0.703	12.3%	[32]
2.	MetAm/PBr ₃ /PVPy	Perovskite	5.1	0.7	5.3% (indoor)	[37]
3.	PPV/ZnO	Hybrid cell	1.14	0.18	1.1%	[38]
			Photocatalytic Hydrogen generation			
4.	PANI/CdSe	Electrolyte 0.5 mmol L ⁻¹ Na ₂ SO ₄	Stability 30 h	H ₂ production Rate >9 mmol h ⁻¹ g ⁻¹ _{cat}	AQY	Ref. [39]
5.	PPE/TiO ₂	0.1 M Na ₂ SO ₄	25 h	228 μmol h ⁻¹	--	[40]
6.	SAO/Pd-TD	Water (Triethanolamine as sacrificial donor)	30 h	1.3 × 10 ⁴ μmol h ⁻¹ g ⁻¹	2.46%	[41]
			Nanogenerators			
7.	PVDF-HP/NaTFSI with PPB	Device type Thermoelectric	Output +20 to -6 mV K ⁻¹	Power/Energy density 2.08 μW cm ⁻² and 833.1 μJ cm ⁻²	Stability 50 cycles	Ref. [42]
8.	PVDF-co-TFE/PZT	Piezoelectric	15 V (Output voltage)	0.75 mW cm ⁻²	63 foot steps in 2 min	[43]
9.	PDMS/SrBaTiO ₃	Triboelectric	280 V (Output voltage)	90 μC m ⁻² (Charge density)	11,000 cycles in ~36 min	[44]

The photovoltaic performances of the polymer/metal oxide hybrid devices are mostly inferior when compared to those of the polymer/fullerene device utilizing the same polymers [45]. The incomplete infiltration of polymers into the pores of the metal oxide layer, poor morphology, and low charge migration behavior of metal oxide are the main factors that affect the optimum charge separation and the exciton-diffusion length of the interfacial region. The issue associated with polymer infiltration can be solved by using polymers of higher molecular weight with polar head groups. These polymers have a great affinity for the polar surface of metal oxides [46]. The alternate strategy is to grow the polymer within the pores of the metal oxide from the soluble monomeric precursors. The ZnO-polyphenylenevinylene-based (PPV) polymer composite synthesized by the approach shows an excellent EQE value of 25% [38]. The poor device performance due to the irregular morphology of the metal oxides can be overcome by growing well-defined vertical structures through the templating methods. The vertically aligned ZnO nanorod arrays synthesized by the sol-gel approach exhibit a higher EQE value of 15% when compared to that of the ZnO nanoparticles using the same P3HT polymer and similar device conditions (Figure 2c) [47]. Moreover, the low charge-recombination rate in the interfacial region is a crucial factor in achieving enhanced device performances. In general, the rate of charge recombination of polymer/TiO₂ is in the range of 100 μs for the uniformly distributed composite material. The lower charge-recombination rate can be achieved in the polymer/TiO₂ composite by shifting the conduction band of TiO₂, thereby enhancing the charge separation effectively. It is accomplished by incorporating a monolayer of molecules having a permanent dipole moment over the metal oxide surface. For example, coating a monolayer of a substituted benzoic acid derivative over the TiO₂ surface yields higher photocurrent due to the suppressed charge recombination [48]. Here, the monolayer of the dipole physically separates the charges before their recombination. The poor charge-transport rate is also a limiting factor. Tin oxide can serve as a better candidate as it has a higher electron mobility than that of TiO₂ and ZnO.

2.1.2. Semiconducting Polymers and Inorganic Nanocrystals-Based Composites

The homogeneous mixing of porous metal oxide with the polymer layer is more challenging to achieve superior power conversion performances [49]. The problem of complete infiltration of metal oxide can be overcome by blending the inorganic nanocrystals with the donor polymers, and it is also possible to achieve this in a single solution-processing step. This approach provides the maximum pool of donor-acceptor interfaces to obtain optimum charge separation and mobility. For this purpose, solution-processing quantum dots or nanoparticles with different morphologies and high electron affinity are widely used to improve the charge transfer abilities of the polymers (donors) with relatively poor ionization

potentials. For example, nanoparticles made of group II-VI elements such as CdSe and PbS are considered potential candidates for hybrid solar cells [49]. The photophysical properties of these nanoparticles can easily be tuned by controlling the morphology and size of the particles during the synthetic process itself. When the hybrid device with P3HT as a donor and CdSe nanoparticles as an acceptor is assembled, the maximum PCE achieved is 1.7% by using the AM 1.5 sun-stimulated radiation [50]. Further, the blend of the PPV donor polymer and the CdSe with a tetrapod morphology showed an improved PCE of >2.1% under similar light illumination conditions (Figure 2d) [51]. In addition to metal selenides and sulfides, metal bromide-based Perovskite nanocrystals (for example, methylammonium bromide (MetAm-Br) and PBr_3) are also utilized to prepare polymer composite materials for solar cell applications. A composite of polyvinylpyrrolidone and MetAm/ PBr_3 nanocrystal is synthesized in the form of a microfibrous mat via an electrospinning technique (Figure 2e) [37]. The light absorption characteristics of the MetAm/ PBr_3 /PVPy fibrous mat are further improved by the PMMA layer, which also enhances the chemical stability of the MetAm/ PBr_3 nanocrystals. The composite material is employed as a luminescent solar concentrator for Si-solar cells, and the MetAm/ PBr_3 /PVPy fibrous mat with a PMMA layer shows a maximum PCE of 3% for the geometrical factor of 1.4 (Table 1). Moreover, the fabricated cells exhibit a PCE of ~5.3% under indoor conditions with white light illumination.

Further enhancements in the PCE are achieved by replacing the homopolymers with the copolymers to increase the light-absorbing ability of the donor up to the wavelength of 600 nm. In order to extend the absorbing nature of the copolymer-based active layer beyond 600 nm, PbSe nanocrystals with a narrow band gap are employed to harvest the near-infrared photons [52]. Later, the toxic CdSe and PbSe materials in the hybrid cells are replaced with ZnO or TiO_2 nanocrystals as acceptor components. However, the overall photocurrents obtained by the device employing ZnO or TiO_2 are comparatively lower due to the larger optical band gap. For instance, the blend comprising functionalized PPV polymers and ZnO nanocrystals shows only 1.4% PCE under AM 1.5-stimulated radiation [53]. Similarly, the hybrid device with P3HT or MEH-PPV polymer and TiO_2 nanoparticles or nanorods delivers the PCE with less than <1% [54,55].

Though the polymer/nanocrystal blends show superior photovoltaic performances than those of the polymer/metal oxide film structures, several issues need to be resolved to achieve higher performance in next-generation devices. The capping agents used to prevent agglomeration and to improve the solution-processing of nanocrystals usually minimize charge separation and transport rates. To overcome this issue, the insulating capping agents are replaced by the ligand-exchange approach [56] or employing a mixture of solvents during the synthetic step to maximize the dispersion ability of nanocrystals [57]. The thermal annealing of the polymer/nanocrystal composites above the glass transition temperature of the polymer can improve the charge-carrier mobility due to the reorganization of the polymeric chain towards better interfacial contact [58].

2.2. Photocatalytic Hydrogen Production

Photocatalytic hydrogen production by splitting water is a fascinating strategy to harvest and store solar energy in the form of chemical energy such as renewable hydrogen [59]. It is an excellent source of sustainable clean energy, and it has very high specific energy when compared to gasoline and lithium-ion batteries. Storage, as well as portable hydrogen, is a primary material for fuel cells [60] that convert chemical energy into electricity with a byproduct of water and zero carbon emissions. In this method, water is used as the starting material, and a photocatalyst is employed to break the water molecule with the help of solar energy. The properties of the photocatalyst determine the faradaic efficiency (the ratio of the number of moles of hydrogen produced to the total amount of charge supplied by the photocatalyst) [61]. Varieties of photocatalysts have widely been utilized to produce green hydrogen including semiconductors, organic dyes, and composite materials [62].

In this section, the conducting polymer and the inorganic semiconductor/metal-based photocatalysts for hydrogen production are discussed.

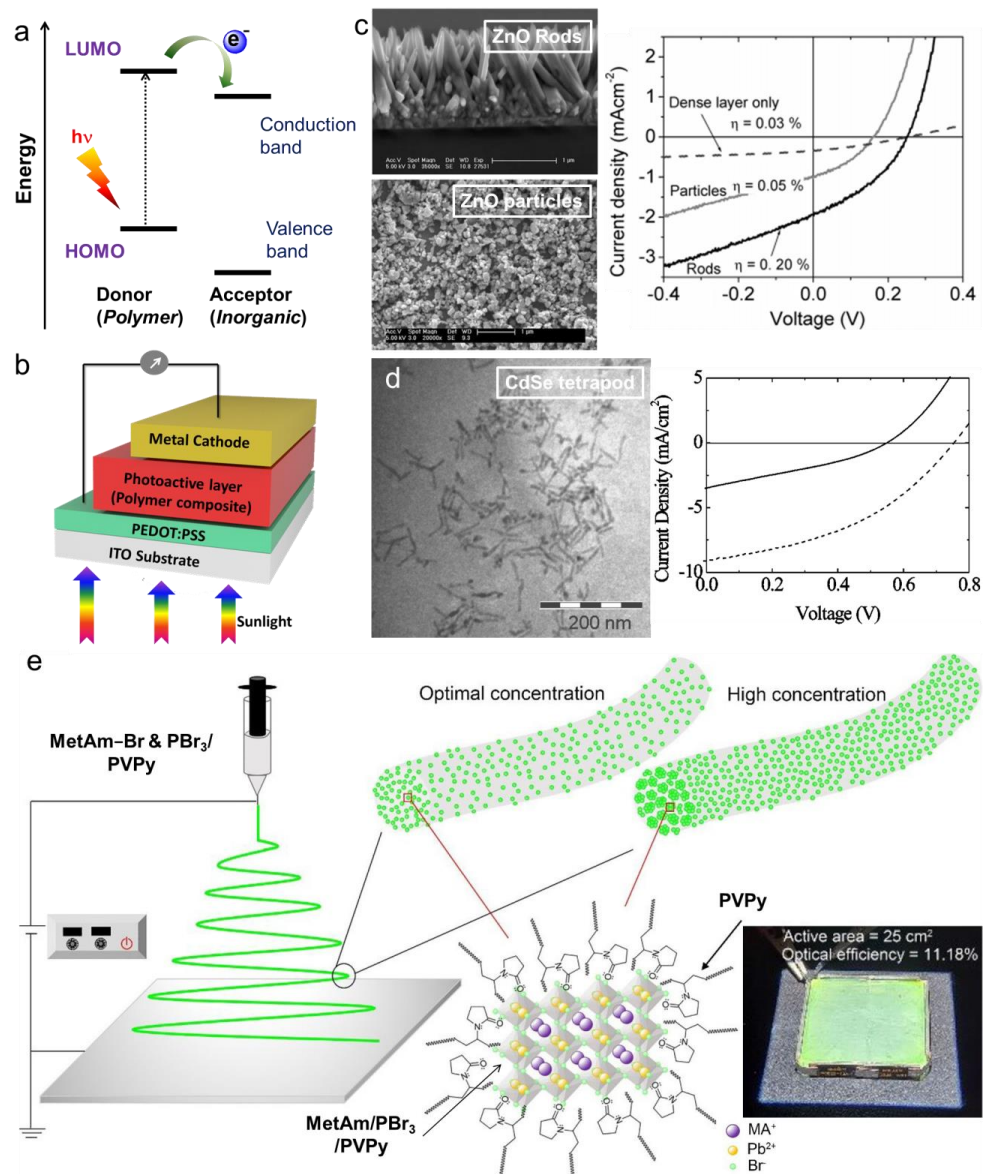


Figure 2. (a) Schematic representation showing the light absorption by the donor followed by the photo-induced electron transfer process of the polymer-inorganic composite. (b) Typical structure of a hybrid solar cell composing polymer/inorganic composite as active material. (c) SEM images of ZnO rods and ZnO nanoparticles, and the *I*-*V* characteristics of solar cells consisted of the ZnO composites [47]. (d) TEM image of CdSe tetrapods and its photovoltaic performance (*I*-*V* curves) [51]. (e) Preparation of a MetAm/PBr₃/PVPy fibrous mat via the electrospinning method and a photograph of a Si-solar cell with the MetAm/PBr₃/PVPy fibrous mat and PMMA layer as luminescent solar concentrators [37].

Inorganic Nanocrystals/Metal/Metal Compounds and Conducting Polymers/Polymer Blends-Based Composites

Among a variety of inorganic semiconductors, cadmium selenide (CdSe) is extensively utilized for this purpose [63]. The band gap of CdSe lies in the range of 2.4 eV and is more appropriate for light absorption that results in photo-induced charge separation. However, the pristine CdSe nanostructures are not very stable because of the weaker surface bond of these structures. The instability of these structures can be improved by combining them

with several conducting polymers, such as PANI (polyaniline), PPy (polypyrrole), and PEDOT. For example, the PPy/CdSe and PANI/CdSe composites have a better ability to inject holes into the highest-occupied molecular orbital (HOMO) of the polymer after absorbing the light energy (Figure 3a) [64]. Among these composites, PANI/CdSe shows the maximum hydrogen production rate of $>9 \text{ mmol h}^{-1} \text{ g}^{-1}_{\text{cat}}$ (Table 1). On the other hand, a composite of PANI/TiO₂ prepared by in-situ polymerization in the presence of TiO₂ possesses a doubled hydrogen production rate than that of the pristine materials [65]. The improved photo-induced charge transfer kinetics of the composite in the interfacial region are the main reason for the better photocatalytic activity. Further, the polyphenylene-acetylene-based polymer (PPE) is covalently attached to the surface of TiO₂ nanoparticles via ester bond formation (Figure 3b,c) [40]. The composite photocatalyst with 4% PPE/TiO₂ exhibits a hydrogen production rate of $228 \mu\text{mol h}^{-1}$ at the irradiated wavelength of 420 nm (Table 1). The well-overlapped energy levels of PPE polymer and TiO₂ and the very close proximity of the covalently bound PPE over the surface of TiO₂ are responsible for the better hydrogen production rate and stability (Figure 3d).

A composite of NaTaO₃ with PANI produces a two-times higher amount of hydrogen for the two hours of light irradiation than that of pristine NaTaO₃ [66]. The NaTaO₃ and PANI interfaces exhibit a low rate of charge recombination, which results in higher photocatalytic activity. Further, a ZnS composite with 40% PANI possesses a four-times higher hydrogen production rate of $>6700 \mu\text{mol h}^{-1} \text{ g}^{-1}$ than ZnS alone [67]. Due to the higher quantum efficiency of ZnO over TiO₂, it is also used for polymer composites. The nickel-doped ZnO has a high concentration of *p-n* heterojunction and achieved a rate of $558 \mu\text{mol h}^{-1} \text{ g}^{-1}$ [68]. Composing the PANI with ZnO leads to a higher light-absorbing ability and harvests most of the visible light region. Similarly, a ternary composite of MoS₂/PANI/CdS heterostructures shows an optimum hydrogen production rate with only a small amount of MoS₂ (4%) and PANI (5%) components [69]. The ternary photocatalyst possesses higher light absorption and an increased charge-separated lifetime, which leads to better photocatalytic activity. In addition to inorganic semiconductors, a lithium polyelectrolyte (Li-PE) consisting of donor-acceptor-type semiconducting organic chromophores such as bithiophene and difluoro biphenyl is also utilized to prepare heterojunctions with graphitic carbon nitride (*g*-C₃N₄) [70]. The composite of Li-PE/*g*-C₃N₄ serves as an effective photocatalyst without co-catalyst, and it delivers a hydrogen production rate of $1932 \mu\text{mol h}^{-1} \text{ g}^{-1}$ with stable activity. Further, it exhibits an apparent quantum yield of 7.9% at the light wavelength of 420 nm. The better photocatalytic hydrogen production rate of Li-PE/*g*-C₃N₄ is attributed to the improved interfacial charge transfer between the significantly overlapped energy levels of Li-PE and *g*-C₃N₄ (Figure 3e). It is further attributed to the higher water wettability due to the presence of lithium sulphonate groups, which maximizes the accessibility of water molecules to the reaction sites.

The incorporation of noble metals in the matrix of conducting polymers has been shown to be an effective way to improve the photocatalytic hydrogen production rate. Both components impart their advantages to the enhanced activity of the photocatalyst. The conducting polymers expand the light-absorbing region in the solar spectrum, and the noble metal nanoparticles accept separated charges, thereby reducing the rate of charge recombination. For instance, the Pd nanoparticles deposited over the TiO₂/PPy exhibit a three-times higher hydrogen production rate when compared to that of the binary composite (TiO₂-0.5 wt%Pd) [71]. Among a series of ternary composites with different weight percentages of the individual components, the TiO₂/0.5 wt%Pd/0.6 wt%PPy shows a very low charge-recombination rate, which is confirmed by the quenching of photoluminescence of the composite material. The optimum photocatalytic activity of ternary composites can be explained as follows: The PPy polymer absorbs light and undergoes the $\pi-\pi^*$ transition. The photoexcited electrons are injected into the conduction band of TiO₂ and then reach the Pd metal nanoparticles. At the same time, the photoexcited TiO₂ transfers holes into the highest-occupied molecular orbital of the PPy polymer effectively. Similarly, the Pd nanoparticle-coated microporous polymeric structures (Pd-TD), comprising triphenylamine

and dibenzothiophene groups, are composited with a strontium aluminum oxide-based ($\text{Sr}_4\text{Al}_{14}\text{O}_{25}:\text{Eu, Dy, B}$; SAO) long-glow phosphorescent material [41]. The SAO/Pd-TD composite exhibits a higher photocurrent response of $\sim 0.16 \mu\text{A cm}^{-2}$ when compared to the pristine individual components (Figure 3f). A high hydrogen production rate of $1.3 \times 10^4 \mu\text{mol h}^{-1} \text{ g}^{-1}$ is observed for the composite with an apparent quantum yield of 1.02% (Table 1). It is attributed to the effective utilization of irradiated light with the help of long-glow phosphorescence material. To further enhance the light-harvesting characteristics of photocatalysts, metal nanostructures with surface plasmon resonance (SPR) are considered better candidates. The SPR-active silver nanoparticles deposited over the graphitic carbon nitride are employed as photocatalysts along with PANI structures [72]. It exhibits a hydrogen production rate of $210 \mu\text{mol h}^{-1} \text{ mg}^{-1}$. The SPR activity of Ag nanoparticles in the ternary composite provides increased light absorption and efficient photo-induced charge transfer kinetics at the interface.

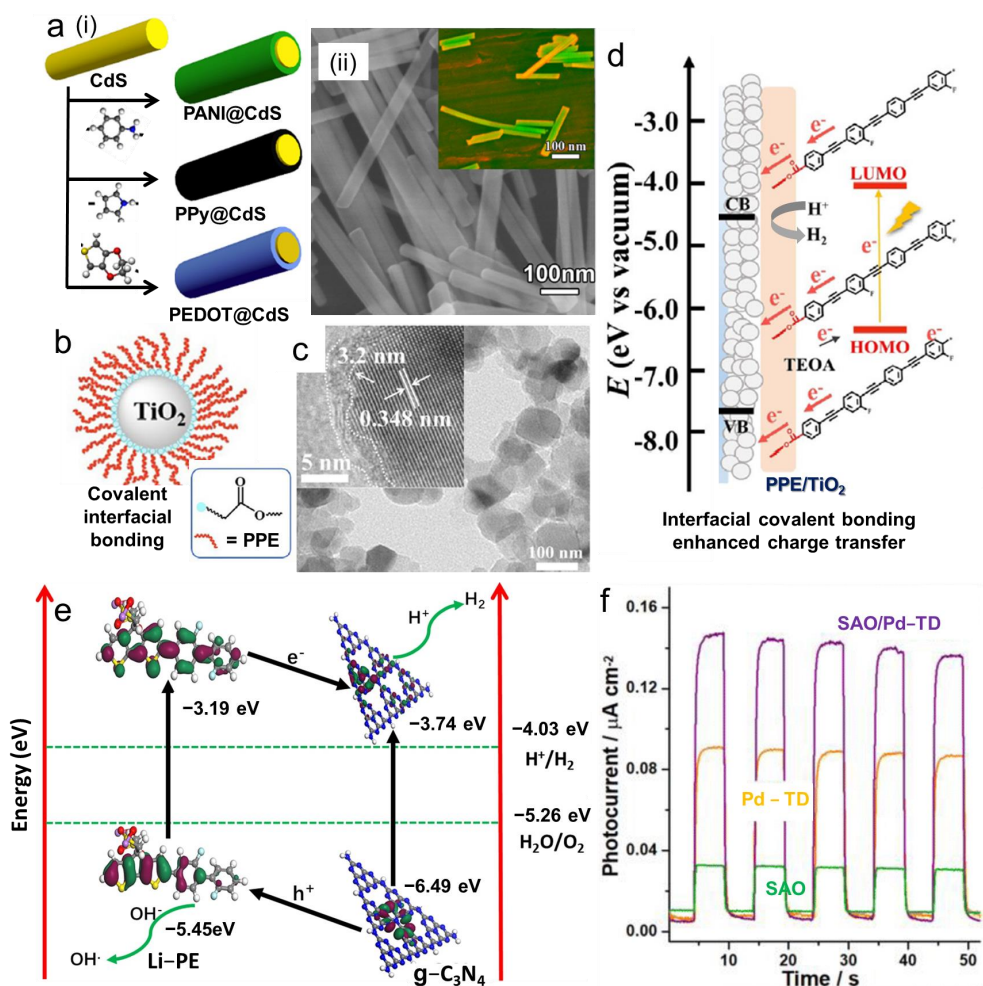


Figure 3. (a) Schematic representation showing (i) the preparation of CdS/polymer-based composites (polyaniline (PANI), polypyrrole (PPy), and poly(3,4-ethylenedioxythiophene) (PEDOT) with cadmium sulfide (CdS) and (ii) the TEM image of the CdS/PANI composite (the inset shows the overlay of secondary and backscattered electron images) [39]. (b) Structure of TiO_2 nanoparticles with polyphenylene acetylene-based polymer (PPE) connected via interfacial covalent bonding and (c) their TEM image [40]. (d) Pictorial representation of photocatalytic hydrogen production of PPE/ TiO_2 composite in the presence of an aqueous solution of a sacrificial reagent (Triethanolamine; TEOA). (e) The energy level positions of Li-PE/g- C_3N_4 with respect to those of the hydrogen evolution reaction and the charge transfer processes of the Li-PE/g- C_3N_4 composite upon photocatalytic hydrogen production [70]. (f) Photocurrent response of the SAO/Pd-TD composite along with the individual components [41].

2.3. Energy Nanogenerators

Nanogenerators are devices that convert the thermal/mechanical form of energy achieved through physical changes into electricity [73]. There are three types of nanogenerators, which include thermoelectric [74], piezoelectric [75], and triboelectric [76]. The thermoelectric nanogenerator harvests the thermal energy from the environment and converts it into electricity, whereas the piezoelectric and triboelectric nanogenerators convert the energy from stress and mechanical friction into electricity, respectively. These nanogenerators have potential applications mainly in micro/nanodevices working with self-power systems and smart wearable sensors for medical applications [77]. In this section, the polymer composite materials employed for the various nanogenerator devices are discussed.

2.3.1. Polymer Composites for Thermoelectric Devices

Most of the heat (a thermal form of energy) generated from natural sources as well as from industries and machinery is unused and dissipated into the atmosphere [74]. On the other hand, an enormous amount of energy input is needed to cool the sophisticated machines and living promises. In this context, thermoelectric (TE) devices have potential applications in various fields. The TE devices harvest the wasted thermal energy and convert it effectively into usable electric energy. The basic components of a TE device are *n*-type (electrons are responsible for conductivity) and *p*-type (migration of holes conducts electricity) materials as unicouples (Figure 4a). In an actual TE device, several tens to a few hundreds of these unicouples are connected in series (electrically), and they are thermally parallel too. When one side of the device is exposed to the thermal source and the other side is relatively low temperature, a potential difference is created across the unicouple modules, and the charge carriers start to move from the higher temperature end to the low temperature end—it is defined as the ‘Seebeck effect’. The TE materials can be evaluated based on a few parameters such as electrical conductivity (σ), Seebeck coefficient (α —represents the potential difference created from the temperature difference, $\Delta V / \Delta T$), and thermal conductivity (κ). The performance of the TE device is characterized by the dimensionless parameter ZT, as given in Equation (1).

$$ZT = T \frac{\sigma\alpha}{\kappa} \quad (1)$$

The TE materials employed for industrial applications (smelters, power stations, and boilers) usually have a temperature difference (ΔT) in the range of 200 to 1000 °C. The alloyed inorganic materials such as PbSeTe/Te [78] or Bi₂Te₃/Sb₂Te₃ [79] exhibit excellent performances for high-temperature applications. Due to toxicity and metal scarcity, alloyed metal-based materials are slowly being replaced with organic or polymer-based materials [80]. However, these materials have a low thermal conductivity in the range of $<1 \text{ W m}^{-1} \text{ K}^{-1}$, electrical conductivity ($<10^4 \text{ S cm}^{-1}$), and Seebeck coefficients ($\sim 10^3 \mu\text{V K}^{-1}$). Because of the thermal instability of these organic materials over 300 °C, the operational temperature of the TE devices made of organic or polymer-based materials is usually below 250 °C, which is more suitable for portable and lightweight applications. Apart from the operational temperature, the other parameters (σ , α , and κ) of the organic-based materials can be improved by compositing with inorganic metal nanoparticles, carbon nanomaterials, and semiconductors. For example, insulating (polystyrene) or conducting (PANI or PPy) polymers can be employed along with inorganic (bismuth telluride) or carbon nanomaterials (fullerenes/carbon nanotubes) for TE applications. When the TE composite is prepared, the important parameter that should be considered is the Fermi level of individual components. The well-matched Fermi level is necessary to lower the energy barrier of the charge carriers.

In the case of conducting polymers, polymer blends containing two different kinds of polymers or organic small molecules are employed to optimize the ZT values [80]. When the PANI is blended with an insulating polymer such as polystyrene or poly(methylmethacrylate,

PMMA), the conducting PANI nanowires are evenly distributed in the insulating polymer matrix. However, the resultant polymer blend exhibits a low Seebeck coefficient of $<8 \mu\text{V K}^{-1}$ at 27°C with a power factor of $6 \times 10^{-6} \text{ W m}^{-1} \text{ K}^{-2}$. To further improve the ZT values, a polymer blend of P3HT and P3HTT is mixed with an electron acceptor small molecule (tetrafluorotertracyanoquino-dimethane) [81]. The polymer composite materials show an improved Seebeck coefficient value of 450 vs. $10 \mu\text{V K}^{-1}$. Furthermore, when a naphthalenedicarboximide-based polymer is doped with a dihydro benzimidazole molecule, the composite demonstrates an *n*-type TE behavior with an excellent α value of $-850 \mu\text{V K}^{-1}$ [82]. It is attributed to the formation of better heterojunctions composed of polymer and organic molecule phase domains with the optimum interfacial regions. Similarly, the polymer composite comprising PVDF, hexafluoropropylene (HP), sodium (trifluoromethanesulfonyl)imide (NaTFSI), and tris (pentafluorophenyl)borane (PPB) exhibits dual *p*- and *n*-type ionic thermoelectric behavior [42]. The all-solid-state thermoelectric device made up of PVDF-HP/NaTFSI delivers a wide range of thermopower from +20 to -6 mV K^{-1} (Table 1) based on the concentration of PPB in the composite (Figure 4b). When the concentration of PPB is 2.5 mM, the composite shows a thermopower of 13 mV K^{-1} , where it is -6 mV K^{-1} with a maximum concentration of 1.5 M (Figure 4c). The conversion of *p*-type ionic thermoelectric behavior to *n*-type behavior is attributed to the Eastman entropy change of NaTFSI in the composite materials.

Polymer composites with inorganic materials such as PbTe and Bi_2Te_3 also show enhanced TE properties. A composite of PEDOT:PSS polymer with PbTe nanoparticles is prepared to yield the crystalline nanorods of PEDOT polymer doped with semiconductor particles. With an optimum loading of PbTe (30 wt%), the composite achieves an impressive Seebeck coefficient of $-4088 \mu\text{V K}^{-1}$ with a power factor value of $\sim 1.5 \mu\text{W m}^{-1} \text{ K}^{-2}$ [83]. Furthermore, polymer composites composed of carbon nanomaterials, such as carbon nanotubes, are also employed to improve the thermoelectric characteristics. For example, a composite of PEDOT: PSS, single-walled carbon nanotube (SWNT), polyvinyl alcohol (PVA), and imidazolium-based sulphonyl imide salt is prepared to fabricate a flexible thermoelectric device with higher mechanical stability [84]. The assembled device possesses a higher tensile strength of 4.2 Gpa and delivers a high power factor of $106 \mu\text{W m}^{-1} \text{ K}^{-2}$. The improved interfacial interactions, such as hydrogen bonding and ionic- π interactions among the individual components, are responsible for the higher mechanical stability and thermoelectric behavior. Further, an SWNT composite with a polythiophene co-polymer comprising platinum acetylides units (PTH-Pt) is utilized for thermoelectric application [85]. The composite of PTH-Pt/SWNT possesses a higher electrical conductivity of $2 \times 10^3 \text{ S cm}^{-1}$ and the fabricated device displays the highest power factor of $\sim 377 \mu\text{W m}^{-1} \text{ K}^{-2}$ (Figure 4d). The better thermoelectric performances of the composite material are ascribed to the various strong interfacial interactions such as $p\pi(\text{Pt})-p\pi(\text{SWNT})$ and $d\pi(\text{PTH})-p\pi(\text{SWNT})$ between the polymer backbone and SWNT structures (Figure 4e).

2.3.2. Polymer Composites for Piezoelectric Devices

Piezoelectric (PE) devices harvest energy in the form of mechanical vibration or stress and convert it into electricity [75]. The piezoelectric effect (defined as a process of electric charge generation when mechanical stress is applied) is an important phenomenon utilized in piezoelectric devices to convert mechanical energy into electricity. PE devices have a simple configuration, the ability to be integrated into complex systems, and higher energy conversion efficiency. In principle, the piezoelectric effect can be explained based on the stimulated imbalance in the charge distribution of the ordered materials. There is an equilibrium between the opposite charges of lattice structures. When mechanical stress is applied to the lattice, an irregularity is induced among the charges or dipoles present in that lattice of PE material. The disrupted charges due to the stress are separated and create a charge density at the surface of the PE material, which is later collected by the external circuit. The PE properties of the materials depend on the symmetry of the materials. In general, materials without centrosymmetry exhibit the piezoelectric effect. In other words,

the materials should show polarization to acquire the PE effect. The technique of inducing the PE effect in the materials is called ‘poling’, which uses a strong electric field at the curie temperature of that particular material. The poling process aligns the electric dipoles in a specific orientation with respect to the applied electric field direction. After this process, the materials have permanently aligned polarization, thereby exhibiting PE behavior. The PE effects can be classified into direct (D_i) and converse (ε_k) effects, which are expressed in the form of equations as given below:

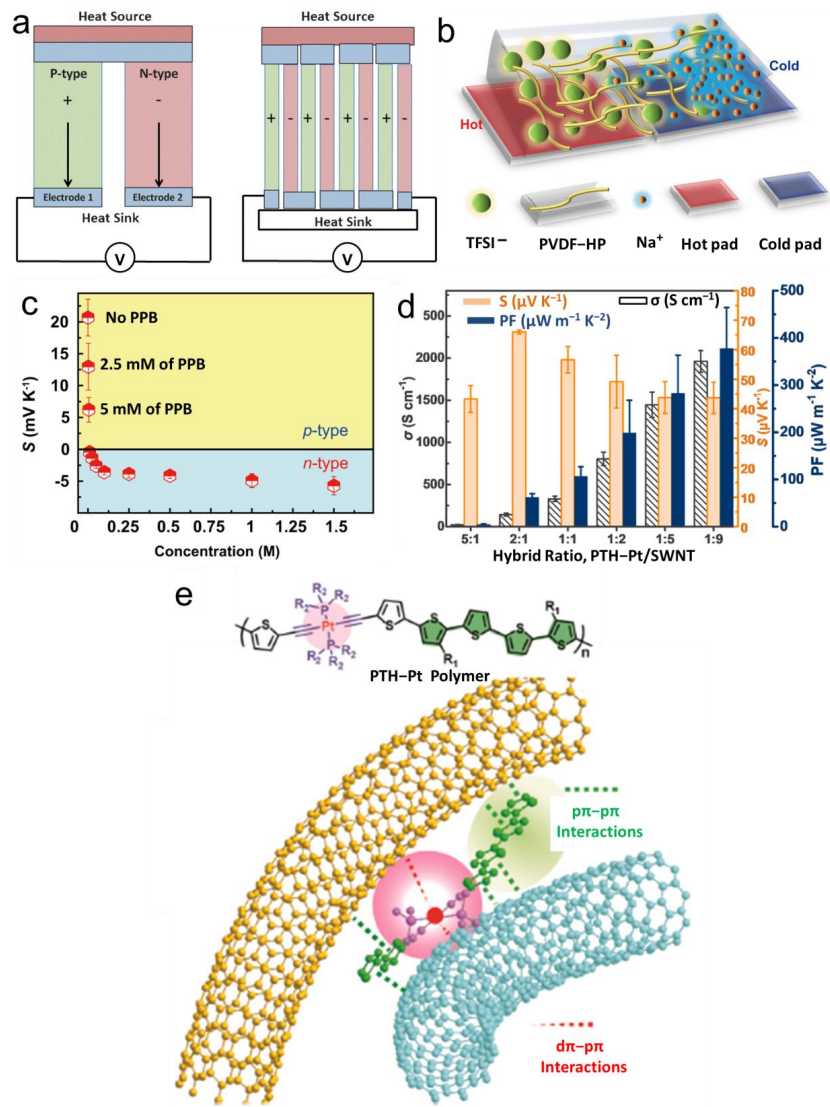


Figure 4. (a) Device structure of a typical thermoelectric device with single and multiple unicouples [86]. (b) Schematic representation showing the distribution of components of the PVDF-HP/NaTFSI composite during the thermoelectric generation [42]. (c) A plot of thermopower vs. concentration of PPB in the composite material of PVDF-HP/NaTFSI. (d) Thermoelectric performances of the PTH-Pt/SWNT composite [85]. (e) Chemical structures of the PTH-Pt polymer and the schematic representation showing the various interactions of the PTH-Pt/SWNT composite.

$$D_i = e_{ij}^{\sigma} E^j + d_{im}^d \sigma_m \quad (2)$$

$$\varepsilon_k = d_{jk}^c E^j + S_{km}^E \sigma_m \quad (3)$$

The dielectric displacement (D_i) and the mechanical strain factor (ε_k) are dependent on the applied electric field (E_j), mechanical stress (σ_m), piezoelectric coefficients of materials

(d_{im}^d & d_{jk}^c), dielectric permittivity (ϵ_{ij}^σ) and elastic compliance (S_{km}^E) of the matrix. The superscripts (i , j , and k) represent three coordinates of the materials, and the subscript (m) symbolizes the shear motions.

A wide variety of ceramic thin films (for example, barium titanate, and BaTiO₃) have been employed for the PE devices. However, these ceramic materials have several disadvantages, such as being fragile, having poor flexibility, and having low voltage coefficients. Alternatively, polymers such as polyvinylidene fluoride, polyimides, polyurethanes, and polylactic acids and their composite materials find enormous applications in PE devices [87]. In particular, the composite materials with piezoelectric ceramic and polymers have a synergistic effect, comprising the PE behavior of the ceramics and the structural flexibility of the polymers, when compared to that of the pristine materials. A composite of lead zirconate titanate (Pb(Zr_{0.52}Ti_{0.48})O₃; PZT) ceramic particles (size of ~100 μm) with PVDF polymers shows a maximum piezoelectric coefficient of 14 pC N⁻¹ (d₃₃) with the polarization of 9 × 10⁻² μC cm⁻² [88]. Furthermore, a nylon textile modified with the PVDF-co-TFE (trifluoro ethylene)/PZT composite (Figure 5a) is employed to fabricate a wearable PE device and used to monitor human motions (foot stepping) under various stress conditions (Figure 5b) [43]. An output voltage of 15 V and an output current of 0.35 μA are achieved with the faster stepping motions. Similarly, PVDF composites with 1D BaTiO₃ structures are also utilized as PE active materials. The uniform distribution of ceramic particles in the polymeric structures determines the energy output value. It can be achieved by using organic small molecules such as dopamine, which improves the homogeneous distribution of BaTiO₃ in the PVDF matrix. With the dopamine (1 vol%)-functionalized BaTiO₃, the polymer composite delivers the highest energy output of more than 6 J cm⁻³ with the maximum breakdown strength (340 MV m⁻¹) [89]. The incorporation of polydopamine with >2 vol% into the BaTiO₃/PVDF composite also results in higher output voltage and sensitivity [90]. The PE device composed of a wearable textile integrated with the 2 vol%-polydopamine/BaTiO₃/PVDF composite operates in a diverse range of applied stresses of 0.2 to 19 N and has sensitivities of 0.38 V N⁻¹ (for output voltage) and ~44 nA N⁻¹ (for output current; Figure 5c). In addition, the PVDF composite with calcinated BaTiO₃ exhibits a better dielectric constant (166) and piezoelectric coefficients (d₃₃; 25 pC N⁻¹) [91]. The piezoelectric properties of the polymer composite are found to be greatly enhanced after compositing with semiconducting materials such as ZnO, TiO₂, and Fe₃O₄. The piezoelectric composite of functionalized PVDF and ZnO (20%) nanoparticles exhibits superior flexibility with an excellent polarization of 15 mC m⁻² at 60 MV m⁻¹ [92]. When the TiO₂-decorated MWNTs are reinforced with a PVDF polymer matrix, the resultant ternary composite demonstrates excellent PE behavior with a maximum piezoelectric coefficient of >40 pC N⁻¹ (d₃₃) [93].

2.3.3. Polymer Composites for Triboelectric Devices

Similar to thermo- and piezo-electric systems, triboelectric devices transform the energy in the form of friction into usable electrical energy [94]. Unlike piezoelectric materials, which have minimum options to tune the material properties that are limited to the symmetry of the systems, triboelectric materials have multiple ways to achieve the optimum materials for this purpose [95]. The triboelectric devices operate under the principle of electrostatic induction resulting from contact electrification. When two materials having different electronic properties come into contact with each other, charge transfer occurs between these materials. The thermodynamic driving force of the charge transfer is dependent on the material properties. If two metal sheets having different work functions come into contact with each other, the charge transfer process will not happen until the Fermi levels of the electrons being transferred are the same everywhere [17]. In the case of metal and ceramic interfacial contact, charge transfer occurs at the interface based on the ‘thermionic-emission effect’ (defined as the process of charge transfer due to the temperature difference between the regions). When the metal comes into contact with the polymer surface, mechanical forces such as friction or rubbing generate a difference in the surface

potential of these materials through charge separation and transfer. Further, the direction and the amount of surface potential variations are defined as “triboelectricity”. Based on the triboelectric behaviors of various materials, a ‘triboelectric series’ has been developed that predicts the ability of the materials to accept or lose the charge when they are in contact with each other. The material that gains a charge easily is called tribo-negative, while the one that loses the charge is called tribo-positive material.

Usually, triboelectric devices possess two kinds of dielectric (or one-dielectric/one-insulator type) materials, which are connected to the external circuit via electrodes. When the two dielectric materials are in contact, no electron is flowed to the external circuit because of the fully balanced opposite charges over their surface. Once these two materials are physically separated, the charges on their surface induce the respective charges at the electrodes, which is referred to as ‘electrostatic induction’. A periodic potential difference is generated across the electrodes during the continuous separation and contact motion of the triboelectric materials. The resultant electric field strength (E) and the potential difference (ΔV) of the active materials can be represented by Equations (4) and (5), as given below:

$$E = \frac{Q}{S \varepsilon_0 \varepsilon_r} \quad (4)$$

$$\Delta V = E_1 d_1 + E_2 d_2 + E_{air} x(t) \quad (5)$$

The efficiency of triboelectric materials is mainly dependent on the dielectric constant (ε_r ; ε_0 is the permittivity of vacuum), surface area (S), and the amount of transferred charge (Q). The best pair of materials for better triboelectric performance is the material placed at the extreme top and bottom of ‘the triboelectric series’. Polymer blends of surface-functionalized polymers serve as better candidates for triboelectric applications [87]. For example, the electro-spun polymer nanofibers of polyacrylonitrile (polyAN; PAN) and PVDF are utilized to prepare wearable fabrics [96]. The triboelectric device assembled with poly-AN and PVDF fabrics is employed for ‘breath monitoring’ due to the higher flexibility of the nanofiber-based fabric and greater filtration capability for very tiny particulates. The continuous physical contact and separation of poly-AN and PVDF fabrics upon inhalation and exhalation events generate the electrical output from the device (Figure 5d). Further, when the combination of poly(trifluoroethyl methacrylate (negative electrode) and poly(L-lysine) (positive electrode) with the well-organized packing of polymer chains is used as active material over the elastic PDMS flexible films, the enhanced dielectric constant leads to improved triboelectric performances [97]. The triboelectric device fabricated on the PDMS support exhibits an output of $>160 \text{ mA m}^{-2}$ and 4.8 V and 38 mA m^{-2} and 5.6 V upon contact and separation events, respectively. Similarly, a device composed of poly-(L-lysine) as a positively charged material and polyethylene terephthalate coated with a functionalized silane compound as a negatively charged material displays a maximum open-circuit potential of 300 V and a current density of 250 mA m^{-2} upon a force of 0.5 MPa is applied [98]. The polymer composite of PDMS with the SrBaTiO₃ microparticles is employed to convert the human stepping motion into electricity via the flooring system (Figure 5e) [44]. The PDMS composite with 10 wt% of SrBaTiO₃ exhibits a device output voltage of 280 V, a current of $>8 \mu\text{A}$, and an aerial capacitance of $90 \mu\text{C m}^{-2}$ (Table 1). It is attributed to an enhanced dielectric constant of >1170 at 100 Hz of applied frequency. The above triboelectric device is more suitable for large-area mechanical energy harvesting into electricity upon integration with the energy-storing supercapacitor towards futuristic sustainable footpath lighting systems.

In addition to titanate-based inorganic materials, a composite of poly(methyl methacrylate) polymer reinforced with aluminum oxide (AlOx) nanoparticles has also been employed for triboelectric devices. It provides comparable performances with a short-circuit transferred charge of more than $50 \mu\text{C m}^{-2}$ as that of titanate-based polymer composites [99]. The improved device performances are attributed to the optimum electrical properties of the polymer matrix achieved through the homogeneous distribution of AlOx particles. Similarly, silver (Ag)-based nanoparticles [100] or nanowires [101] are also uti-

lized to prepare the polymer composites for this purpose. For example, the composite of natural rubber with Ag nanoparticles shows better triboelectric performance depending on the capping agent (sodium dodecyl sulphate or cetyltrimethylammonium bromide) than that of the pristine natural rubber [100]. The natural rubber composite of Ag nanoparticles with cetyltrimethylammonium bromide exhibits a higher interfacial polarization and enhanced dielectric constant, resulting in higher device output ($>0.8 \text{ W m}^{-2}$) when compared to sodium dodecyl sulphate as a capping agent. The smaller size of the nanoparticle as well as the interparticle distance are attributed to the improved triboelectric performances. Additionally, the presence of Ag nanoparticles imparts anti-bacterial activity if the triboelectric device is integrated with the shoe insole to harvest the mechanical energy via foot-stepping motions. Further, the incorporation of single-walled carbon nanotubes and reduced graphene oxide into the Ag-based polymer composites improved the triboelectric performances [101,102]. In addition, when the reduced graphene oxide is introduced into the polyimide polymer matrix, a maximum output power of more than 6 W m^{-2} is achieved under the vertical contact-separation mode. It is attributed to the effective capture of triboelectrically generated electrons by the graphene nanosheets [103]. Similarly, the MoS_2 nanosheet-distributed polyimide polymer matrix outperforms the polyimide/graphene composites and delivers the highest output power of 25 W m^{-2} because of the effective trapping of electrons, thereby suppressing charge recombination at the interfaces [104].

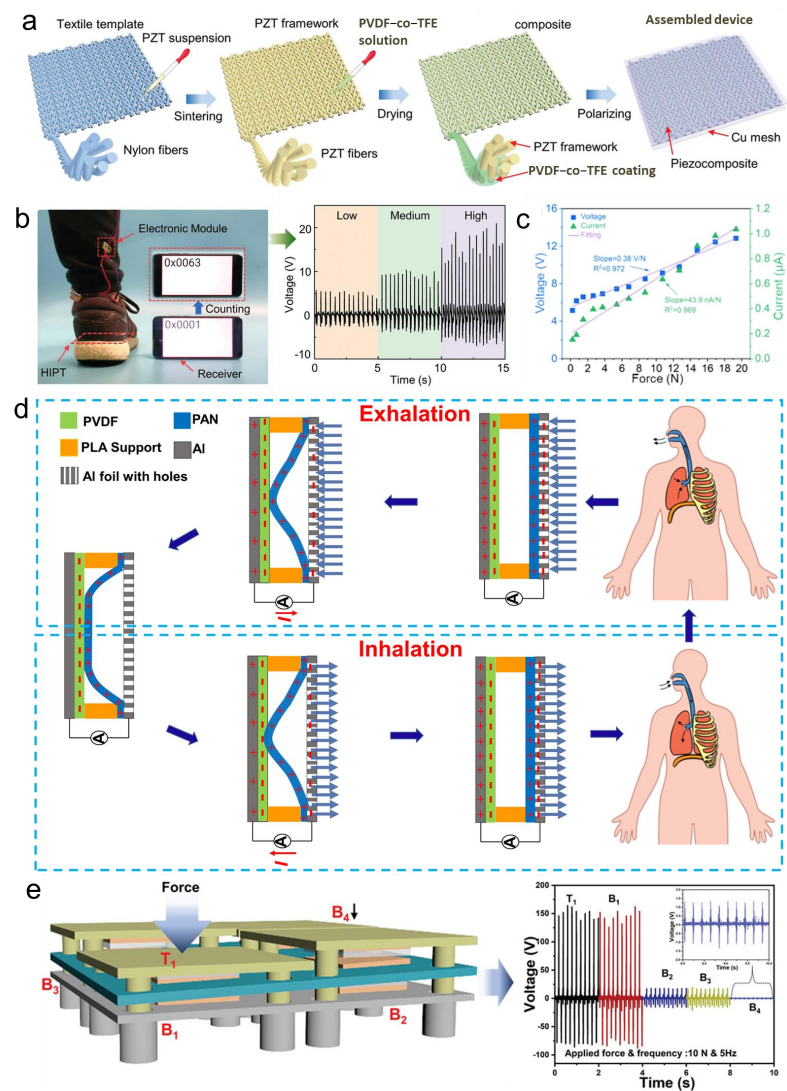


Figure 5. (a) Preparation of a piezoelectric polymer composite comprising PVDF-co-TFE and $\text{Pb}(\text{Zr}_{0.52}\text{Ti}_{0.48})\text{O}_3$; PZT [43], (b) photograph and plot of voltage vs. time showing the real-time monitoring

of foot-stepping under various stress conditions via the piezoelectric device made-up of PVDF-co-TFE/PZT composite. (c) A plot of voltage and current vs. applied force obtained from the PE device composed of 2 vol%-polydopamine/BaTiO₃/PVDF composite [90]. (d) Schematic representation showing the working principle of the triboelectric device composed of polyAN and PVDF composite, which is integrated with a face mask for ‘breath monitoring’ [96]. (e) Pictorial representation of a triboelectric device consisting of PDMS composite with 10 wt% of SrBaTiO₃ to harvest the mechanical energy through the foot stepping motions and its triboelectric performance [44].

3. Interfaces of Energy Storage Materials

3.1. Supercapacitors

An electrochemical capacitor, also known as an ultracapacitor/supercapacitor, is considered an important energy storage device and has widely been used in electric vehicles, portable electronic devices, and so on [18]. They differ from their counterparts, namely batteries, in terms of charge/discharge time, stability, and energy/power densities. Electrochemical capacitors usually possess high charge/discharge rates, power density, and cyclic stability when compared to other batteries. The electrochemical capacitors can be classified based on their charge storage mechanism: (i) electrochemical double-layer capacitors (EDLC), which adopt the electrical double-layer behavior of electrode-electrolyte interface by electrostatic adsorption/desorption of charges (non-faradaic process) over the electrode surface in the presence of an applied potential; (ii) pseudocapacitors that utilize fast redox reactions over the surface of active electrode materials such as inorganic compounds (metal hydroxides/oxides/sulphides), conducting polymers, and their composites, in addition to the double-layer contributions. The pseudocapacitors usually deliver a higher specific capacitance than that of the EDLC due to the charge transfer reactions (Faradaic processes) at the electrode-electrolyte interface. Among the diverse electrode materials developed for this purpose, polymer composite materials have been proven to be the better candidates for next-generation lightweight and flexible energy storage devices. Polymers with a π-conjugated backbone are electrically conductive, referred to as conducting polymers, and they have widely been employed for the development of various electrode materials for supercapacitors. The disadvantages of conducting polymer-based electrode materials are poor long-cycle life, higher charge transfer resistance, and electrochemical degradation into soluble products. The above issues, however, can be addressed by combining them with other materials. The composite materials consisting of carbon nanomaterials, metal compounds, MXenes, and TMDs, along with PANI, PPy, and PTH, were studied extensively, and furthermore, they showed better electrochemical performances than those of the pristine polymers. In this section, various polymer composites of carbon nanomaterials and metal compounds are elaborated with a few representative examples.

3.1.1. Polymer Composites of Carbon-Based Materials

A variety of carbon porous materials, such as carbon black, activated carbon, and carbon fibers, are used as templates to synthesize polymer composite materials with improved conductivity, surface area, and a low degree of agglomeration of polymeric particles [18]. The different spectroscopic methods, including X-ray photoelectron spectroscopy, are commonly used to characterize the interaction between the polymer and the carbon material. It is proven that the carbon materials act as only templates, and there are no chemical interactions between the polymeric structures and the carbon materials. Further, the composite materials of conducting polymers and carbon nanomaterials such as carbon nanotubes and graphene derivatives have extensively been studied as electrode materials for supercapacitors. The polymer composites prepared by the chemical polymerization method show a higher molecular weight, poor solubility in electrolytes, and better chemical stability. In general, they are synthesized by the polymerization of monomers (aniline, pyrrole, and thiophene) with the help of oxidizing agents (NH₄)₂S₂O₈, KMnO₄, FeCl₃, and K₂Cr₂O₇) over carbon nanotubes or graphene derivatives such as graphene or reduced graphene

oxide. The lack of a high degree of homogeneity and continuity of polymeric structures are the disadvantages of the chemical polymerization method. For example, when carbon nanotubes with a diameter of 20–30 nm are used for the chemical polymerization of aniline/pyrrole monomers, the average size of one-dimensional polymeric composite structures of 50–200 nm can be obtained. The agglomeration of polymeric structures into particles is also possible due to the preferential growth of their structures over the surface of carbon nanomaterials.

The physical and chemical properties of the polymer-carbon nanomaterial composites primarily depend on the different synthetic parameters such as the concentration ratio of monomers/oxidizing agents, the pH of the medium (for PANI/PPy polymers synthesized in water), reaction time, and temperature [105]. These parameters have an immense effect on the electrical conductivity and molecular weight of the resultant polymer composites. Ultrasonication has a great influence on the structural and electrical properties of composites. The pristine carbon nanomaterials have lower dispersion abilities in most of the solvents due to the strong noncovalent interactions among them. It has been shown that ultrasonication improves the crystallinity and electrical conductivity of polymer composites with carbon nanotubes because of the effective mixing of heterogeneous components. The electrochemical performances of these polymer/carbon nanomaterial composites mainly depend on the morphology, porosity, conductivity, crystallinity, and degree of solubility in the electrolyte solution. For example, the composite of PPy deposited over the carbon nanofibers possesses a specific capacitance of 545 F g^{-1} at a 200 mV s^{-1} scan rate [106]. The composite delivers a high capacitance when the polymer content is increased to a certain percentage due to the inclusion of more redox-active groups in the composite material [107].

The PANI/SWNT composite with 73 wt% of PANI structures shows a specific capacitance of 463 F g^{-1} [108]. The PEDOT polymeric structures over the carbon nanotubes with a polymer content of 15 wt% exhibit a better capacitance of 95 F g^{-1} when compared with the pristine carbon nanotubes (CNTs) ($<10 \text{ F g}^{-1}$) and PEDOT (80 F g^{-1}). The higher specific capacitance and the better charge/discharge rate of the polymer composites are mainly attributed to the increased accessibility of electrolyte ions to the active site of the electrode materials with a minimum charge-transfer resistance [109]. Further, the electrochemical performance of these composites is also influenced by the nature and concentration of the electrolyte ions. The PEDOT/CNT structures deliver a higher capacitance of 120 F g^{-1} in $1.0 \text{ M H}_2\text{SO}_4$ aqueous electrolyte, whereas it is only 80 F g^{-1} and 60 F g^{-1} in 6 M KOH and acetonitrile solutions of 1.0 M TEABF_4 electrolytes, respectively [110]. In addition to the nature of the electrolyte, the physical properties, such as surface area and porosity, of carbon nanomaterials also affect the specific capacitance of the polymer composites. The MWNTs with higher surface area and pore volume show improved electrochemical performance over the SWNTs with the same kind of polymeric counterparts [111]. To show the application of these polymer composites in practical prototype supercapacitor devices (two-electrode configuration), polymer/CNT composites have widely been employed as electrode materials for symmetric as well as asymmetric (hybrid cells) devices. The two-electrode cell composed of PANI/CNT as the cathode and bare activated carbon as the anode exhibits higher specific power and specific energy in an acidic electrolyte solution ($1 \text{ M H}_2\text{SO}_4$) [112]. Among various polymer/CNT composites, PANI/PPy with carbon nanotubes showed higher specific capacitance and stability in aqueous electrolyte solutions. In addition to the conducting polymers, structural polymers such as polyamides are also utilized to prepare composites with CNTs. For example, nylon/spandex fibers are coated with the CNTs to create polymer core-CNT sheath-like structures (Figure 6a). The nylon/CNT composite shows excellent stretchability, mechanical stability, and crack resistance upon coiling (Figure 6b) [113]. These coiled polymer composite fibers could easily be woven into fabric substrates for wearable devices (Figure 6c). The coiled nylon/CNT fibers prepared even at 300% of applied strain show an aerial capacitance of $\sim 12 \text{ mF cm}^{-2}$ at a scan rate of 0.01 V s^{-1} . The device also exhibits a higher capacitance retention of >98% after 100 full stretch/release cycles (Table 2). Further, carbon nanofibers made up of

carboxylmethylated cellulose and chitosan are employed to prepare PEDOT-based porous polymer composite structures [114]. A 3D ultralight-weight aerogel with a density of $\sim 12 \text{ mg cm}^{-3}$ is created from the carboxylmethylated cellulose and chitosan polymers, and it is subsequently loaded with PEDOT structures via in-situ polymerization (Figure 6d). The porous PEDOT/polymer composite delivers a specific capacitance of 77 F g^{-1} at a scan rate of 1 mV s^{-1} (Table 2).

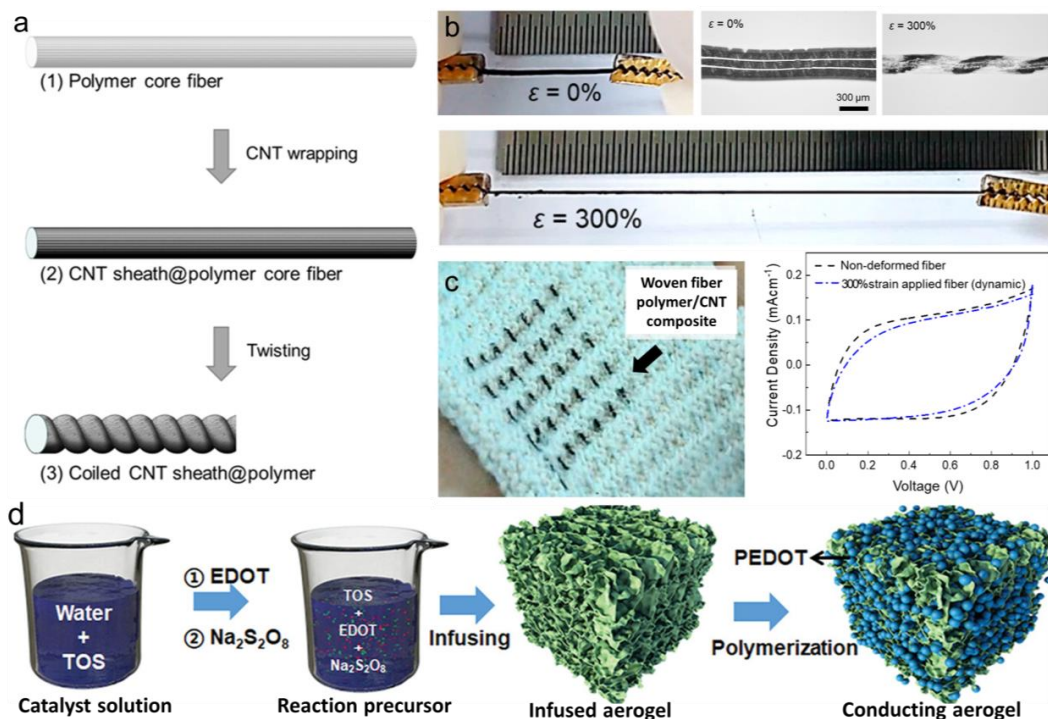


Figure 6. (a) Preparation and (b) optical and microscopic images of nylon/CNT composite fiber under different applied strain conditions [113]. (c) Photograph showing the woven fabric with the nylon/CNT composite fibers and the CV of the fiber supercapacitor device under different applied strain conditions. (d) Preparation of porous carboxylmethylated cellulose and chitosan composite aerogels with PEDOT structures [114].

Table 2. Selected list of polymer composite materials for energy storage devices.

S.No.	Polymer Composites of Energy Storage Devices					
1.	Material Nylon/CNT	Electrolyte 0.1 M Na_2SO_4	Supercapacitors Operating voltage $\sim 1 \text{ V}$	Specific capacitance $11.89 \text{ mF cm}^{-2} 10 \text{ mV s}^{-1}$ (Areal capacitance)	Cyclic stability 94.2% after 100 times of the full stretch-release cycle	Ref. [113]
2.	Cellulose-Chitosan derived CNF/PEDOT	Sat. Na_2SO_4	0.6 V	77 F g^{-1} at 1 mV s^{-1}	--	[114]
3.	PPy/rGO-melamine (Hybrid supercapacitor)	2 M ZnSO_4	1.6 V	130 mAh g^{-1} at 0.2 A g^{-1}	$\sim 91\%$ after 3000 compression/release cycles	[115]
4.	Poly-TEMPO/SWNT	LiPF6 in EC/DMC (1:1)	Metal-ion Batteries Operating voltage $\sim 2 \text{ V}$	Specific capacity 98 mA h g^{-1} at 10 C	Cyclic stability $>95\%$ capacity retention (2000 GCD cycles)	Ref. [116]
5.	Acrylic resin/silver nanopowder	Hydrated solid NaOH	$\sim 1 \text{ V}$	100 mAh g^{-1} at 20 mA g^{-1}	$>97\%$ at 100th cycle	[117]
6.	PEDOT/Vanadium oxide	3 M $\text{Zn}(\text{CF}_3\text{SO}_3)_2$ aqueous solution	$\sim 1.2 \text{ V}$	370 mA h g^{-1} at 500 mA g^{-1}	$>80\%$ capacity retention after 1000 cycles of GCD	[118]
Composite Polymer Electrolyte for LIBs						
7.	Electrolyte Material Pluronic polymer and piperidinium bromide	Electrolyte type Polymer-gel	Specific capacitance/capacity 441 F g^{-1}	Energy density 16.8 Wh kg^{-1}	Cyclic Stability 92% after 10,000 cycles at -30°C	Ref. [119]
8.	LLTO/PDOL	Polymer-membrane	155 mA g^{-1} at 0.1 C	--	70% after the 350 GCD cycles	[120]
9.	LLZrNb/polydopamine	Polymer-inorganic	$>150 \text{ mA h g}^{-1}$ at 0.1 C	362 Wh kg^{-1}	$>80\%$ after 100 cycles of GCD	[121]

Two-dimensional carbon nanomaterials such as graphene derivatives (graphene oxide, graphite nanoflakes, and reduced graphene oxide) have also been utilized to prepare polymer composite materials as electrode materials for supercapacitors. Polymers of PANI, PPy, PTH, and *p*-phenylenevinylene (PPV) [122] are successfully incorporated into these graphene-based composites. The electrochemical polymerization method is considered an effective technique to prepare composites of PPy/graphene. The composites prepared through the above method show higher specific capacitance and better electrochemical stability [123,124]. Further, the PPy/graphene composite synthesized through chemical polymerization showed a relatively lower capacitance (482 F g^{-1} at 0.5 A g^{-1}) [125], when compared to the one, prepared through electropolymerization (1510 F g^{-1}) [126]. This is mainly due to the morphological differences between the composites prepared by different synthetic routes. Similarly, the PANI/graphene composite prepared with uniformly distributed pore structures exhibits a substantial increase in the capacitance value. The other factors that have a significant role in the performance are the agglomeration abilities of graphene sheets and the nature and concentration of the electrolyte solution used [127]. A PANI/graphene composite with a microsphere structure possesses a capacitance of $>200 \text{ F g}^{-1}$ at a higher current density of 30 Ag^{-1} , which is higher than that of the pure PANI ($\sim 65 \text{ F g}^{-1}$) [128]. The spherical structures of the graphene sheets with a higher surface area are responsible for the synergistic effects. The formation of three-dimensional macroporous structures of PANI/graphene composites resulted in a higher capacitance of 921 F g^{-1} [129]. Further, microscopic 1D fibrous structures composed of PEDOT:PSS/graphene nanosheets are employed to fabricate flexible supercapacitor devices with PVA gel electrolyte (Figure 7a) [130]. The assembled supercapacitor shows a specific capacitance of 281 F g^{-1} at a current density of 100 mA g^{-1} . It also exhibits better cyclic stability (capacitance retention of $>90\%$ after 5000 GCD cycles) even at sub-zero temperatures of -20°C , which is attributed to the higher ionic conductivity of the electrolyte and faster charge transfer kinetics of microfibrous electrode materials.

The synergistic effect of graphene derivatives in polymer composites is the enhancement of morphological features and the electrical properties of polymer counterparts. These improvements greatly influence the electrochemical performance of the polymer/graphene composites. For example, when the PPy polymer having a surface area of $35 \text{ m}^2 \text{ g}^{-1}$ is mixed with graphene, the resultant composite attains the maximum surface area of $250 \text{ m}^2 \text{ g}^{-1}$ with higher specific capacitance and electrochemical stability. Furthermore, a PPy/rGO polymer composite is prepared over the melamine-based 3D porous sponge material to achieve a compressible zinc-ion hybrid supercapacitor [115]. The device assembled by sandwiching the PPy/rGO-melamine sponge electrode with two zinc foils leads to the effective use of active polymer interfaces (Figure 7b). It delivers a higher specific capacitance and energy of 130 mAh g^{-1} and $>100 \text{ Wh kg}^{-1}$ (Table 2). The compressible supercapacitor possesses 90% of its initial capacity after 3000 cycles of the compression-release process with a strain of 40%. In addition to the graphene derivatives, a graphite-based polymer composite is also employed as a flexible electrode material for symmetrical supercapacitors [131]. The composite of poly(lactic acid) with a conducting graphite powder ($>60 \text{ wt\%}$) is prepared by a slurry casting method and obtained as free-standing electrode material. The symmetrical flexible supercapacitor fabricated with the PVA-KOH gel electrolyte shows an area capacitance of $\sim 2 \text{ mF cm}^{-2}$ at $\sim 0.015 \text{ mA cm}^{-2}$. Further, after 5000 GCD cycles, the device possesses $>99\%$ capacitance retention. The two-electrode devices fabricated using composites of polymer/graphene derivatives delivered excellent energy and power densities.

3.1.2. Polymer Composites of Metal Oxides/Hydroxides/Sulphides-Based Materials

The preparation of polymer composites with various metal compounds (oxides/hydroxides/sulfides) has several advantages for the overall electrochemical performance of the polymer composites [132]. The major issue with pristine conductive polymer-based electrode materials is the considerable volume changes of the polymeric structures during the

charge/discharge processes, which cause reduced cyclic stability and specific capacitance over time. Composing these polymers with metal compounds can prevent the volume change issue by enhancing the mechanical stability, thereby improving the capacitance and cyclic stability. The incorporation of metal compounds into the polymeric structures leads to higher energy density and cyclic stability when compared to the polymer composites prepared from carbon materials and other polymer blends [132]. On the other hand, conductive polymers also have a few positive effects on the performance of these composites with metal compounds. The agglomeration of metal oxides/hydroxides/sulfides is greatly reduced through the noncovalent interactions, which help ensure the uniform distribution of the particles in the polymeric structures. Among several metal oxides, RuO₂ is a widely used transition metal oxide to prepare composites of polymers/metal compounds. For instance, a three-dimensional architecture composed of RuO₂ and PPy polymer shows a capacitance of 302 F g⁻¹ at 0.5 mA cm⁻², which is higher than that of the pristine PPy [133]. The improved electrochemical performance of the RuO₂/PPy composite is attributed to the lower charge transfer resistance at the electrode-electrolyte interfaces of these 3D tubular structures. Further, the low-cost and highly scalable polymer/metal oxide composite can be prepared by replacing the expensive RuO₂ with the relatively cheaper MnO₂. The deposited thin film, comprising MnO₂ and PPy structures directly over the current collector, exhibits a higher specific capacitance (620 F g⁻¹) and cyclic stability when compared to that of the pristine materials [134]. Similarly, PANI/MnO₂ and PEDOT/MnO₂ composites prepared by intercalation and co-electrodeposition methods, respectively, show impressive electrochemical performances. The intercalated PANI structures in between the layered MnO₂ possessed more than 94% of their specific capacitance after several cycles of a charge-discharge process [135]. The PEDOT/MnO₂ composite with the coaxial nanowire architectures demonstrated excellent rate performance (variation of capacitance with the different given current densities during the charge-discharge process). It is found that the composite shows 85% of its capacitance even at the higher current density of 25 mA cm⁻², which is attributed to the synergistic effects of the flexible PEDOT polymer on the solid core structures of MnO₂ [136].

A binder-free electrode composed of PANI/NiO structures with a 3D flower-like morphology is also employed for supercapacitors [137]. The composite architecture exhibits a remarkable specific capacitance (2565 F g⁻¹ at 1 Ag⁻¹) and a rate performance of (70% of its initial capacitance at higher current density). A PEDOT composite with a mixture of NiO and Ni(OH)₂ is also prepared with 3D flower-like structures, and the composite possesses a capacitance of 404 mF cm⁻² at 4 mA cm⁻² and better cyclic stability [138]. The hybrid supercapacitor device fabricated with PEDOT/NiO/Ni(OH)₂ as the cathode and mesoporous carbon as the anode delivered an energy density of 0.011 mW h cm⁻² with an operating voltage of 1.45 V. Further, the other transition metal oxides, namely, V₂O₅, Fe₂O₃, and CoO, are also employed for the preparation of polymer composites for supercapacitors. A PPy/V₂O₅ composite obtained via the electrodeposition method shows a nanowire morphology with a higher surface area [139]. These nanowire composite structures exhibit maximum accessibility of electrolyte ions with lower charge-transfer resistance, which deliver a higher capacitance (412 F g⁻¹ at 4.5 mA cm⁻²). A two-electrode asymmetric device composed of PANI/Fe₂O₃ with a core-shell structure as anode and PANI structures grown over carbon substrate as cathode shows an impressive volumetric capacitance (2.02 mF cm⁻³) and cyclic stability (95% of its initial capacitance after several thousand cycles of the charge-discharge process) [140]. Moreover, a PPy composite with a bimetallic oxide such as NiCo₂O₄ is prepared with a coaxial nanowire structure on a carbon substrate for a flexible supercapacitor device [141]. The coaxial structures possess highly capacitive NiCo₂O₄ core structures and a uniformly distributed PPy coating over them. These core-shell architectures are more suitable for optimum ionic diffusion of electrolytes, which results in higher capacitance, rate performance, and cyclic stability. The flexible supercapacitor device with PPy/NiCo₂O₄ delivers a maximum energy density of 58.8 Wh kg⁻¹ and a power density of 365 W kg⁻¹. In addition to metal oxides and

hydroxides, several metal sulfides, such as NiS_x, CuS_x, and CoS_x, are also used to prepare polymer/metal sulfide composites [142]. A composite of CuS sphere-like structures with PPy coatings exhibits better capacitance and cyclic stability. Similarly, a PPy/NiS/cellulose composite with a fibrous structure delivers a higher capacitance of 713 F g⁻¹ with excellent energy density (239 Wh kg⁻¹) and power density (39 W kg⁻¹) [143].

3.1.3. Polymer Composites of Two-Dimensional Layered Materials

Transition metal dichalcogenides (TMDs) belong to the 2D graphene analogous layered materials, and they comprise diverse 2D materials with a range of electronic properties, from insulators to metallic through semiconductors and semimetals [144]. Due to their exciting physical and chemical properties, they are potential candidates for various applications in the field of materials science. The semiconducting TMDs, namely, MoS₂, WS₂, MoSe₂, and WSe₂, are extensively exploited in the areas of electrocatalysis and energy storage. Like carbon nanomaterials and metal oxides/hydroxides, TMDs have also been utilized to prepare polymer/TMD composites for supercapacitor devices. Preparation of composites from the nanosheets of TMDs with conductive polymers is a constructive approach to overcome the inferior electrical conductivity of these semiconducting 2D-layered materials towards supercapacitors [144]. In an optimum PANI/MoS₂ composite material, the arrays of PANI nanorods are grown over the MoS₂ sheets to achieve a higher surface area for maximum electrolyte accessibility [145]. The PANI/MoS₂ composite possesses a higher specific capacitance of 853 F g⁻¹ at 1A g⁻¹. The better rate performance and cyclic stability of the composite are attributed to the shorter diffusion paths of the electrolyte ions, which maximize the rate of redox reactions at the electrode-electrolyte interfaces. Similarly, a PPy/MoS₂ composite delivers impressive energy (83.3 Wh kg⁻¹) and power (3332 W kg⁻¹) densities [146]. These remarkable energy and power densities are ascribed to the presence of metallic 1T-phase MoS₂, which imparts a strong interfacial noncovalent interaction and a higher surface area of homogeneously distributed PPy and MoS₂ nanosheets. Furthermore, the Mo metal centers of MoS₂ have very strong coordination interactions with the nitrogen atoms of the polymeric backbone, and the various ranges of oxidation states of Mo atoms (+2 to +6) provide an additional pseudocapacitive contribution to the overall specific capacitance of polymer/MoS₂ composite electrodes. A stretchable supercapacitor device composed of a curable copolymer of hexafluoropropylene and vinylidene fluoride-based electrodes with 1T-MoS₂ and PVA-phosphoric acid-gel electrolyte is also fabricated [147]. The polymer composite electrode material is printed over the metal current collector (Au substrate) toward wearable device structures (Figure 7c). The assembled flexible supercapacitor with 50% of the applied strain exhibits a better specific capacitance of ~30 mF cm⁻² at 0.2 mA cm⁻² and an energy density of >3 mWh cm⁻³. It retains more than 80% of its relative capacitance even at the applied strain of 40% during GCD cycles (Figure 7c).

In addition to TMDs, another class of 2D layered materials such as transition metal carbides/nitrides/carbonitrides (MXenes with a general formula of M_{n+1}X_nT_x; 'M' represents a transitional metal, 'X' indicates a C/N element, and 'T' represents a functional group –OH/-F ion) have also been employed for the polymer composite materials for supercapacitors [148]. The MXene layers are obtained by solution-phase exfoliation of the bulk MAX materials ('A' represents the IIIA or IVA elements). Though the MXenes have interesting physical and electronic properties, the inferior electrochemical characteristics, namely, low capacitance and poor rate capability, could be overcome by incorporating the conductive polymers into the MXenes materials [148]. For example, a PPy/Ti₃C₂ composite prepared via electrophoretic deposition followed by an electrochemical polymerization method exhibits an aerial capacitance of 109 mF cm⁻² at 1 mA cm⁻² in an acidic electrolyte [149]. The improved capacitance and excellent cyclic stability of the PPy/Ti₃C₂ composite are ascribed to the better 2D ionic diffusion path through the Ti₃C₂ layers and the pseudocapacitive behavior of PPy polymeric structures. Further, the PANI/Ti₃C₂T_x composite prepared through solution exfoliation followed by the chemical polymerization technique exhibits a similar areal capacitance (103.8 mF cm⁻² at 2 A m⁻²) as that of PPy/Ti₃C₂ [150]. A

ternary PANI/Ti₃CT_x/graphene composite delivers impressive energy (42 Wh kg⁻¹) and power (950 W kg⁻¹) densities while assembling an asymmetric supercapacitor device with a carbon electrode as anode [151].

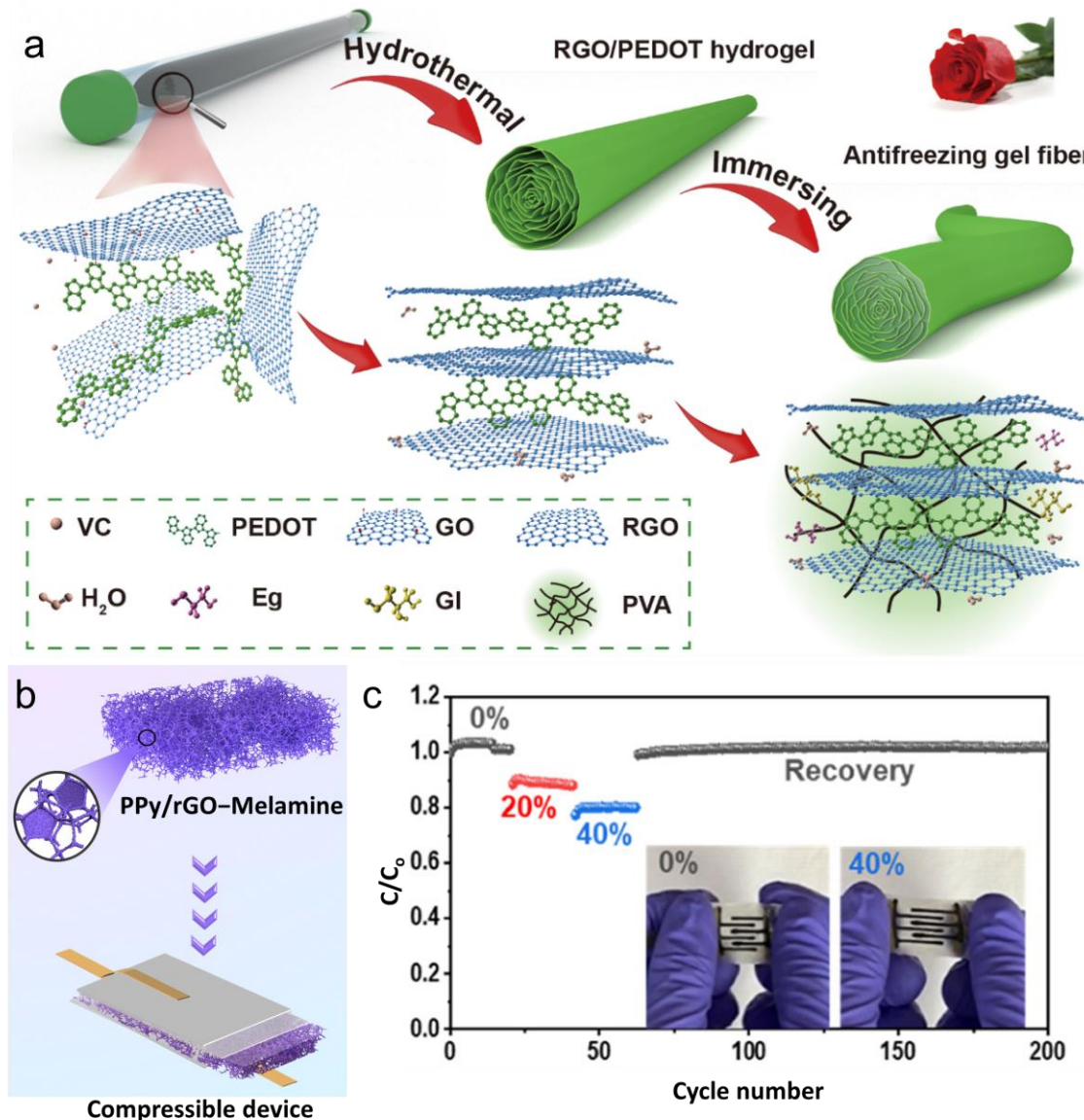


Figure 7. (a) Preparation of 1D microfibers of PEDOT/rGO polymer composite with infused gel electrolyte [130]. (b) Design of a compressible PPy/rGO-melamine sponge-based zinc-ion hybrid supercapacitor [115]. (c) A plot of relative capacitance vs. the number of cycles of a stretchable 1T-MoS₂/fluoride-containing elastomer-based supercapacitor device [147].

3.2. Metal-Ion Batteries

In addition to electrochemical capacitors, metal-ion batteries play a crucial role in electrochemical energy storage. There are several types of metal-ion batteries currently available [152]. Among them, the major rechargeable metal-ion batteries are lithium-ion, sodium-ion, and zinc-ion batteries. The charge storage mechanism of these batteries is mainly dependent on the intercalation or deintercalation of metal ions into or from the cathode and anode electrode materials. Preparation of polymer composites has several advantages for metal-ion batteries, which include (i) minimization of electrochemical degradation of polymeric structures during the electrochemical reactions; (ii) attainment of negligible self-discharge; and (iii) enhancement of electrolyte accessibility to the active sites with a short diffusion path and a very low charge transfer resistance. In this section,

the electrochemical performances of redox-active polymer composite materials towards a variety of metal-ion batteries are discussed.

3.2.1. Polymer Composites for Lithium-Ion Batteries (LIBs)

LIBs are the dominant secondary rechargeable batteries among the other metal-ion batteries due to their higher energy density, long life cycle, and low self-discharge behavior. A variety of polymer composite materials have been used as both anode and cathode materials in the LIBs based on the potential window where the redox reaction of these polymers usually occurs. For instance, composites with PANI, PPy, PTH, PEDOT, and redox-active polymers consisting of carbonyl/imine functional groups also act as electrode materials [153–155]. For example, the copolymers of 3,4-ethylene-dioxythiophene-(EDOT)/thiophene-, thiadiazole- and benzotriazole-based monomeric units are employed to prepare composites with activated carbon towards anode materials [156]. The activated carbon imparts pseudocapacitive behavior to these composites. The polymer composite with the EDOT units shows a higher specific capacity of 372 mAh g^{-1} at 100 mA g^{-1} whereas it is 303 mAh g^{-1} at 100 mA g^{-1} for the thiophene-based composite. The better lithium-ion storage characteristics of the former are attributed to the increased charge transfer kinetics at the polymer-activated carbon interfaces. In addition to activated carbon, one-dimensional carbon nanomaterials such as SWNT/MWNTs are also utilized to make polymer composites. An SWNT composite composed of a tetramethyl-1-piperidinyloxy (TEMPO)-based radical polymer possesses a three-dimensional network-like structure with higher structural stability and electrical conductivity [116]. The Poly-TEMPO/SWNT composite exhibits higher cyclic stability with >95% capacity retention (2000 GCD cycles) and rate capability (Table 2). The higher electrochemical performances are ascribed to the uniform distribution of polymeric chains over the surface of SWNT (Figure 8a), which results in the rapid transport of charges at the interfaces. In addition, a ternary composite of PANI/MWNT/polyoxometalate with different ratios of individual components exhibits a reversible discharge specific capacity of 1000 mAh g^{-1} at 0.5 mA g^{-1} and better cyclic stability [157].

Further, 2D carbon nanomaterials such as reduced graphene oxide have also been used to prepare composites. A polymer comprising anthraquinone sulfide (AS) units is synthesized via an in-situ polymerization method in the presence of reduced graphene oxide [158]. The poly-AS/rGO composite shows a microporous structure with evenly distributed rGO sheets. Because of higher electrical conductivity and favorable morphological features, the poly-AS/rGO exhibits a better specific capacity of 148 mAh g^{-1} at 10 C and capacity retention of 93% after 500 GCD cycles. The porosity of polymer composites is further improved by adopting the coassembly technique followed by the cross-linking strategy [159]. The two-dimensional as well as spherical-shaped composites of polystyrene are prepared with rGO and silica (SiO_2) nanoparticles, respectively (Figure 8b). Then, the cross-linking of the surface polystyrene chains of these polystyrene/rGO and polystyrene/ SiO_2 composites leads to interpenetrated interblock connectivity with plenty of meso/macropores. The etching of SiO_2 nanoparticles further improves the porosity of the 3D hierarchical structures. The resultant 3D-polymer composite serves as a better cathode material for Li-sulfur batteries. The highly porous nature of the composite significantly reduces the polysulfide shuttling effect, thereby enhancing the electrochemical performances. Similarly, PANI/1T-MoS₂/rGO composite serves as a cathode material for LIB in 1M LiPF₆ in ethylene carbonate/dimethyl carbonate electrolyte with fluoroethylene carbonate (FEC) as an additive [160]. The ternary composite exhibits superior cyclic stability in the presence of FEC additives due to the formation of a protective solid-electrolyte interface (SEI) over the electrode material. The SEI is electrically insulating and ionically conductive in nature, which facilitates the proper Li-ion diffusion into the electrode. The PANI/1T-MoS₂/rGO composite with the FEC additive possesses two-fold higher capacity retention after the 400 cycles of charge-discharge when compared to the one without the FEC additive.

3.2.2. Polymer Composites of Sodium-Ion Batteries (SIBs)

SIBs are better alternatives to LIBs in terms of the natural abundance and cost of sodium metal when compared to lithium. In addition, SIBs are more resistant to overcharge problems, unlike LIBs, where the device can be discharged nearer to zero volts, thereby increasing the energy density. A polymer composite composed of polydopamine and carbon nanotubes is prepared over a flexible substrate, and the SIB assembled from the polymer composite material exhibits a higher specific capacity of 213 mAh g^{-1} at 0.05 A g^{-1} with better cyclic stability [161]. Similarly, a composite of functionalized polyvinyl methacrylate polymer with tetramethyl piperidinyloxy groups (PVMA) and carbon nanotubes is employed to address the self-discharge problem associated with SIBs [162]. The device fabricated with the PVMA/CNT composite possesses a stable open circuit potential in a fully charged state over a period of 20 days. The excellent self-discharge resistance and better specific capacity (130 mAh g^{-1}) are attributed to the uniform distribution of polymer coating over the nanotubular structures, which improve the stability of the sodium-ion intercalated/deintercalated state of the device. Further, a PPy polymer doped with $\text{Fe}(\text{CN})_6^{4-}$ complex is utilized to improve the capacity (up to 135 mAh g^{-1}) of SIBs considerably when compared to that of the pristine materials [163]. It is a synergistic effect of the highly reversible Na^+ intercalation/deintercalation process along with the redox contribution of the $\text{Fe}^{2+}/\text{Fe}^{3+}$ pair. In addition to the inorganic complex, an organic-anion-doped PPy is utilized to improve the rate performance and cyclic stability of the SIB device [164]. Further, a composite of acrylic resin and silver nanopowder is employed as a cathode material for sodium-air/water batteries [117]. The reversible electrochemical reaction of sodium metal into sodium hydroxide in the presence of oxygen/water (atmospheric moisture) is responsible for the energy storage characteristics. The silver nanopowder of the polymer composite electrochemically catalyzes the above conversion reactions. The composite cathode exhibits better GCD cyclic performance at a relative humidity of 7% and an operational temperature of 80°C . In addition to that, the composite nanofibers of polyvinyl pyrrolidone and sodium vanadium phosphate (SVP) prepared via electrospinning are utilized as a sodium-ion-rich cathode in a sodium-zinc hybrid aqueous battery [165]. The polyvinyl pyrrolidone polymer of the nanofibers is calcinated into a carbon coating that uniformly wraps the SVP particles. The hybrid aqueous battery with the above calcinated composite electrode and sodium perchlorate/zinc acetate/2 wt% vinylene carbonate electrolyte exhibits a higher operating potential window of $>1.45 \text{ V}$ and cyclic stability of $>84\%$ after the 1000 cycles of GCD. It is also operable at low temperatures and possesses the specific capacities of 94 and 90 mA h g^{-1} at -10 and 20°C , respectively. The introduction of electrolyte additives such as vinylene carbonate not only extends the operating potential window but also serves as a precursor to form a protective solid-electrolyte interface over the electrode material, which effectively prevents the dissolution of SVP particles.

3.2.3. Polymer Composites for Zinc-Ion Batteries (ZIBs)

In the case of ZIBs, a variety of inorganic and organic materials have widely been employed as electrode materials. Low specific capacity, poor rate performance, and cyclic stability are the major issues with the above materials for ZIBs. As we discussed earlier, several conductive polymer composites are also utilized for ZIBs, similar to Li/Na-ion batteries. For example, a composite of PEDOT and vanadium oxide is synthesized with three-dimensionally arranged nanosheet structures through in-situ polymerization of EDOT in the presence of vanadium oxide [118]. Upon utilizing the PEDOT composite as the cathode, the device exhibits a specific capacity of 370 mA h g^{-1} at 500 mA g^{-1} and better cyclic stability with $>80\%$ capacity retention after 1000 cycles of GCD. The synergic effect of mixed-valence vanadium ions (V^{4+} and V^{5+}) and the conducting PEDOT polymeric structures are responsible for the improved electrochemical performances. The formation of dendritic structures of zinc after repeated GCD cycles is a major problem associated with long-term cyclic stability. The protection of the zinc anode by creating a porous polymer membrane at the electrode-electrolyte interface significantly minimizes zinc dendritic

growth. For instance, the polyvinylidene difluoride-based membrane with plenty of zinc-ion channels enhances the electrochemical performance of the polymer-coated zinc anode [166]. In a full device configuration, the above anode possesses a specific capacity of $>110 \text{ mA g}^{-1}$ after $>14,000$ GCD cycles at a high specific current (10 A g^{-1}). The faster zinc-ion kinetics and effective inhibition of dendritic growth are attributed to the improved performance of the modified zinc anodes. In addition to the modifications of the zinc anode, the polymer-incorporated electrolytes [167–169] are also employed to lower the dendritic growth of zinc over the surface of electrodes and to improve the ion-transport properties of electrolytes. An addition of a polysaccharide derivative (hyaluronic acid-glycosaminoglycan) to a zinc sulfate aqueous electrolyte results in dendritic-free electrodes and greater zinc-ion transport properties [170]. The symmetric Zn cell with the polymer additive shows better cyclic stability of >2200 h at 1 mA cm^{-2} current density.

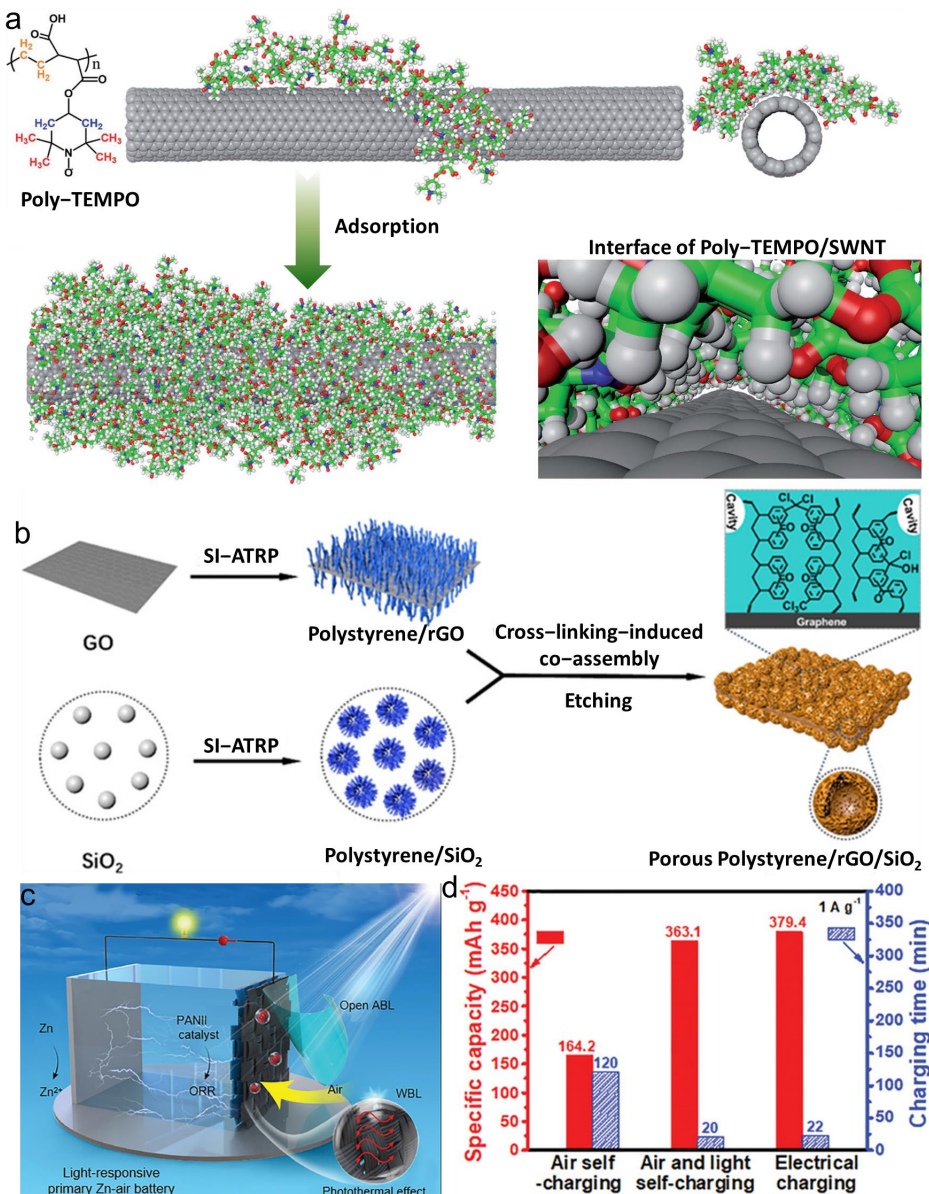


Figure 8. (a) Schematic representation showing the preparation and the interfacial structure of the poly-TEMPO/SWNT composite [116]. (b) Synthesis of a cross-linked polystyrene/SiO₂/rGO composite towards a lithium-sulfur battery [159]. (c) Design of a self-chargeable aqueous zinc-ion battery of polyaniline/carbon fibers (PANI/CF) with multimode-operational capabilities [171]. (d) A plot of the specific capacity of PANI/CF//Zn full cells under various self-charging conditions.

Furthermore, a ternary composite of PANI and PEDOT:PSS with CNTs is used as a cathode material for ZIBs [172]. The polymer composite exhibits a better specific capacity (238 mAh g^{-1} at 0.2 Ag^{-1}) and a higher rate performance in the presence of a polymer-based electrolyte. The improved charge storage characteristics of the device are ascribed to the incorporation of plenty of sulphonate groups (-SO₃H) through the PSS polymer. The sulphonate groups impart a pool of H⁺ ions that enhances the redox reaction of PANI polymers with protonation/deprotonation reactions. The 1D structures of CNTs increase the overall conductivity of the ternary composite electrode. On the other hand, the PANI nanorods grown over carbon fibers (PANI/CF) are also utilized for self-chargeable ZIBs [171]. The different properties, such as reversible redox activity, oxygen-reducing ability, and photothermal activity, of the polymer cathode interface are attributed to the multimode-operational capabilities of the fabricated full battery device (Figure 8c). Precisely, the oxygen-reducing character of the cathode enables the device to self-charge by acting as a zinc-air battery with a specific capacity of 363 mAh g^{-1} (Figure 8d). At the same time, the photothermal character of the cathode increases the capacity to 430 mAh g^{-1} upon irradiation of light at the electrode.

3.3. Polymer Composite Electrolytes for Energy Storage Devices

Electrolytes play a significant role, equally to the electrode materials, in the development of high-performance energy storage devices [18]. Conventional electrochemical capacitors and batteries with liquid electrolytes suffer a lot due to the limited stable operating potential window and safety risk factors such as fire and explosion. Replacing liquid electrolytes with semi-solid/solid electrolytes is an effective strategy to address the above issues [173]. To replace conventional liquid electrolytes, semi-solid/solid electrolytes should possess considerable ionic conductivity, high mechanical strength, and interfacial stability. A few types of semi-solid/solid electrolytes are currently available for energy storage devices, which include inorganic/ceramic, polymer-gel/membrane, and polymer/inorganic composite electrolytes [174]. In this section, the latest advancements in polymer-gel/membrane and polymer/inorganic composite electrolytes are discussed.

Polymer-gel/membrane electrolytes are semi-solid/solid systems comprising salt and polymer as a matrix. In the polymer-gel electrolytes, the salt and the solvent are incorporated into the semi-solid medium by in-situ polymerization of monomers [175]. On the other hand, the polymer-gel/membrane-based electrolytes are achieved by incorporating the salt or infiltrating the salt solution into the three-dimensionally porous polymer membrane structure followed by the removal of any excess unabsorbed electrolyte [176]. In general, the electrolytes prepared via the above methods have better ionic conductivity, avoid electrolyte leakage, and also act as separators between the electrodes. They can be prepared by incorporating a wide range of components, such as ceramic fillers, mixed metal salts, and solvents. Several polymers have been adopted for the preparation of polymer-gel/membrane electrolytes. Among them, the important polymers are polyvinyl alcohol (PVA), polyethylene oxide (PEO), polyvinylidene fluoride (PVDF), and polymethyl methacrylate (PMMA) [174]. The electrochemical performances and the ionic conductivity of these electrolytes depend on the ingredients and also on the physical properties of the polymer matrix, such as porosity and distribution. Liquid-phase casting, gel crystallization, and electrospinning are well-known techniques to prepare these electrolytes. In general, polymer-gel electrolytes mainly lack mechanical stability, especially for flexible supercapacitors or battery devices. However, the thermoreversible gels composed of PVDF polymers with a variety of metal salts have superior ionic conductivity and mechanical stability when compared to those of the other polymers. For instance, the PVDF-based polymer-gel electrolytes [177] prepared with polar solvents, namely, dimethyl formamide/propylene carbonate, could achieve an ionic conductivity of more than $10^{-2} \text{ S cm}^{-1}$ even at sub-zero temperatures. Further, the polymer gel electrolyte based on pluronic polymer and piperidinium bromide/iodide is employed for an aqueous supercapacitor operable even at -30°C [119]. The symmetrical supercapacitors fabricated with the reduced graphene

oxide as electrodes exhibit a specific capacitance of 441 F g^{-1} and 436 F g^{-1} at 25°C for the polymer-gel electrolytes with piperidinium bromide (Pip-Br) and piperidinium iodide (Pip-I), respectively (Table 2). These electrolytes possess the property of ‘inverse melting’- indicating the liquid state at sub-zero temperature and the semi-solid state at ambient temperature, which is the reverse of common liquid behavior upon cooling. It leads to more than 70% capacitance retention even at -30°C for Pip-Br-based electrolytes, whereas it reduces to 32% for Pip-I-based counterparts. It is attributed to the large size of the iodide ion, which shows inferior ionic conductivity and charge transfer kinetics when compared to that of the bromide ion. In addition, a biopolymer-based composite electrolyte consisting of cellulose nanocrystals and polyvinyl ester is also used to prepare polymer-gel electrolytes [178]. It exhibits an ionic conductivity of 1.1 mS cm^{-1} with a cellulose loading of 2 wt%. The strong hydrogen bonding interaction among the cellulose and polyvinyl ester chains leads to a polymer-gel electrolyte with higher mechanical stability. The LIB assembled with the above polymer-gel electrolyte possesses a better tensile strength of $>300 \text{ MPa}$ and delivers a specific capacity of $\sim 120 \text{ mAh g}^{-1}$ at $\sim 0.3 \text{ C}$.

Furthermore, the nanofibrous framework of lithium lanthanum titanate obtained via electrospinning is incorporated into the poly-1,3-dioxolane-based polymeric matrix by in-situ polymerization (LLTO/PDOL; in-situ PLE) [120]. Since the polymerization is carried out in the presence of a sandwiched lithium anode and a lithium iron phosphate cathode, better interfacial contact between the electrode and electrolyte is achieved (Figure 9a). The above lithium-ion battery exhibits a specific capacity of 155 mA g^{-1} at 0.1 C (Table 2) and a capacity retention of 70% after the 350 GCD cycles (Figure 9b). The better conductivity ($\sim 6 \times 10^{-4} \text{ S cm}^{-1}$) and the formation of a LiF-rich solid-electrolyte interface are responsible for improved lithium-ion storage characteristics when compared to the ex-situ-generated polymer electrolyte (ex-situ PLE). Alternatively, a composite polymeric membrane composed of PVDF-hexafluoropropylene, polyethylene oxide, and ZIF-modified Ti_3C_2 is infiltrated with lithium salt ($\text{LiTFSI}/\text{LiPF}_6$) dissolved in a mixture of ethylene carbonate and dimethyl carbonate [179]. It exhibits an ionic conductivity of 4 mS cm^{-1} , tensile strength of 3.8 MPa , and a lithium-ion transference number of 0.76. An assembled $\text{LiFePO}_4/\text{Polymer electrolyte}/\text{Li}$ battery shows a specific capacity of 121 mAh g^{-1} at 5 C and a capacity retention of $\sim 90\%$ after 500 GCD cycles. Similarly, the electrospinning technique is utilized to introduce a zirconium-based metal-organic framework into the nanofibers of PVDF-hexafluoro propylene and polyethylene oxide. These composite fibrous structures are incorporated within a lithium sulphonate-appended polyacrylamide matrix through a photopolymerization process [180]. The LIB fabricated with the above composite electrolyte delivers a specific capacity of 105 mAh g^{-1} at 2 C and a capacity retention of $>98\%$ after the 120 GCD cycles at 0.5 C . In addition, lithium alginate and ZIF-67-composed polyacrylamide-based polymer composite electrolytes are also employed for LIBs [181]. Furthermore, composite polymer membranes serve as an excellent platform to disperse highly brittle ceramic conducting materials and achieve mechanically stable ceramic/polymer membrane electrolytes. For example, lithium lanthanum zirconium oxide (LLZr)-based ceramic conductors are reinforced with PVDF- and hexafluoro propylene and polyethylene oxide [182] matrixes. The polymer composite of LLZr and LiTFSI is converted into a three-dimensional porous membrane via an electrospinning technique (Figure 9c). The 3D porous structure of the composite polymer-membrane imparts greater flexibility, higher thermal stability, and ionic conductivity, which results in faster lithium-ion kinetics and charge transfer (Figure 9d). The $\text{LiFePO}_4/\text{LLZr-Polymer composite electrolyte}/\text{Li}$ battery exhibits a specific capacity of 147 mAh g^{-1} and better cyclic stability with a retention of 99% after 180 GCD cycles.

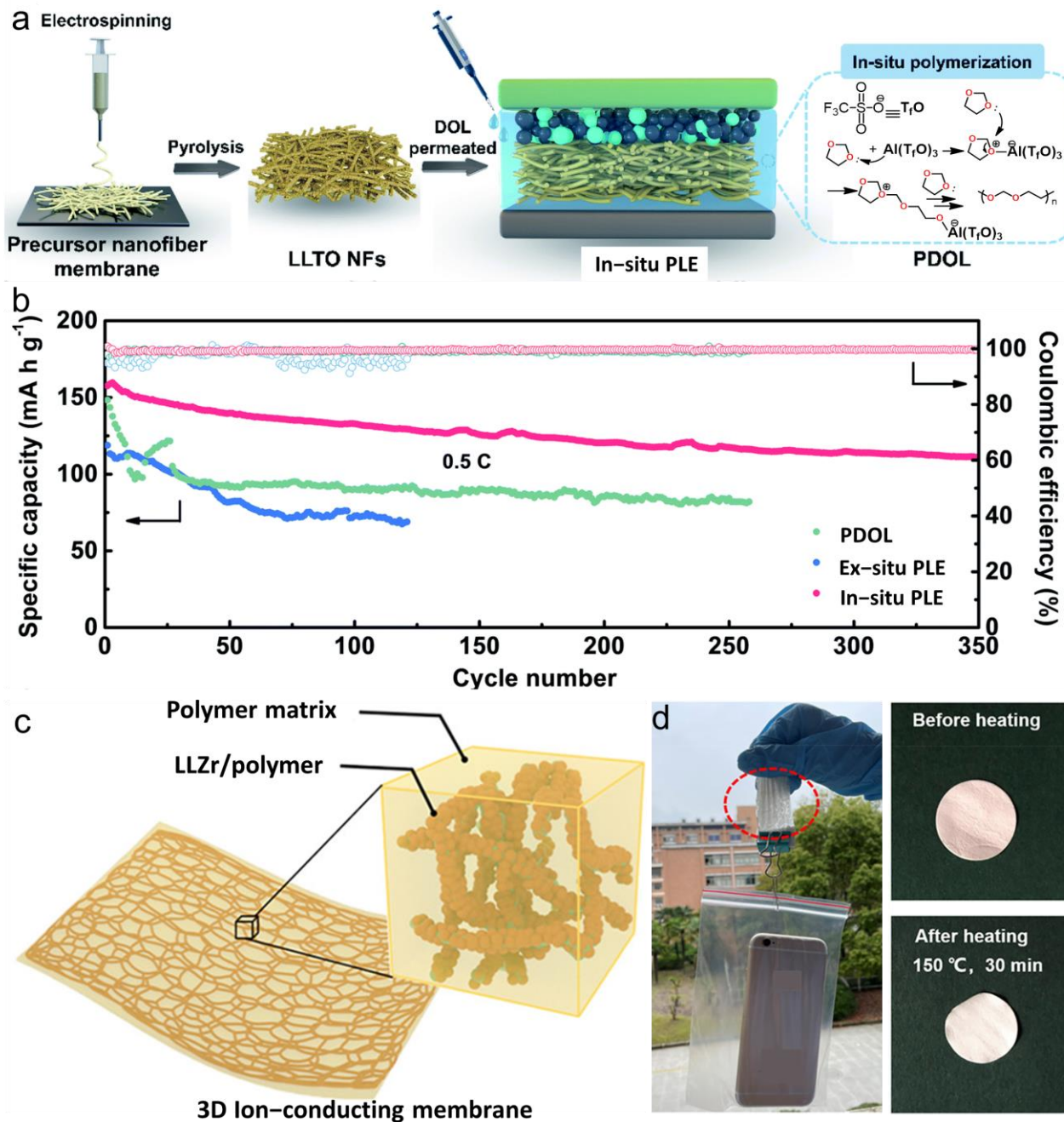


Figure 9. (a) Preparation of in-situ polymerized lithium lanthanum titanate/poly-1,3-dioxolane (LLTO/PDOL) composite electrolyte for LIBs [120]. (b) A plot of the cyclic stability test of various LIBs of LLTO/PDOL with different electrolytic conditions. (c) The structure of the LLZr-based composite polymer membrane and (d) the photographs showing its mechanical and thermal stabilities [182].

On the other hand, though the inorganic electrolytes have excellent ion transport character, physical strength, and stability, inferior contact with the electrode material leads to enormous interfacial impedance [173]. In the initial stages, ceramic particles were employed for composite electrolytes; however, the performances of these electrolytes were unsatisfactory. The development of polymer/inorganic composite electrolytes is inevitable to address these issues [183]. The ion transport properties of the composite electrolytes are mainly governed by the inorganic components. By introducing fillers such as $\text{Li}_{1+x}\text{Al}_x\text{Ti}_{2-x}(\text{PO}_4)_3$ (LATP), $\text{Li}_{0.33}\text{La}_{0.56}\text{TiO}_3$, and $\text{Li}_{6.4}\text{La}_3\text{Zr}_{1.4}\text{Nb}_{0.6}\text{O}_{12}$ -polyethyleneoxide-LiN(CF_3SO_2)₂, the ionic conductivity of the composite polymer electrolytes for LIBs is enormously improved to

$>1 \times 10^{-3}$ S cm $^{-1}$ [184]. For example, the Li_{6.4}La₃Zr_{1.4}Nb_{0.6}O₁₂ (LLZrNb)/polydopamine (PDA) composite electrolyte is developed for all-solid-state LIBs [121]. The polydopamine is coated over the lithium carbonate-free surface of LLZrNb particles through metal (La) and nitrogen atom interactions (Figure 10a). These stronger interactions between LLZrNb and polydopamine lead to better Li-ion transport via the polymer-LLZrNb interfaces. It exhibits a higher Li-ion transference number of 0.6 and a Li-ion conductivity of 0.15 mS cm $^{-1}$ at 25 °C. An all-solid-state LIB assembled with lithium cobalt oxide//LLZrNb-PDA//Li device shows a higher cut-off voltage of 4.5 V, a specific capacity of >150 mA h g $^{-1}$ at 0.1 C, and a specific energy of 362 Wh kg $^{-1}$ (Table 2). It also possesses a capacity retention of $>80\%$ after 100 cycles of GCD, and furthermore, the fully charged device could power around 140 LEDs at the same time (Figure 10b,c). Moreover, particulate ceramics are replaced with ceramic materials having a specific morphology, such as nanowires, nanotubes, and three-dimensional porous structures. For instance, a 3D porous structure composed of a ceramic material such as Li_{1+x+y}Al_xTi_{2-x}Si_yP_{3-y}O₁₂ (LATSCO) is prepared, and it is infiltrated with the cross-linkable polyethylene oxide (PEO) and LiTFSI solution (Figure 10d) [185]. Then, both sides of the composite electrolyte are spray-coated with the polyethylene oxide and LiTFSI mixture to create a trilayer structure of composite electrolyte and polymer coating that acts as a protective layer between the electrode and composite electrolyte (Figure 10d). The trilayer composite electrolyte demonstrates higher stability towards the fracture of the electrolyte film and prevents the short-circuiting of the device when compared to the conventional non-porous polymer-ceramic composite electrolyte. Similarly, a lithium phosphorous sulfide (LiPS)-based polyethyleneoxide/polypropyleneoxide (PEO/PPO) composite electrolyte is synthesized via the solution-precipitation method with evenly distributed polymer-LiPS interfaces [186]. The conductivity of the PEO/PPO-LiPS composite electrolyte reaches 0.3 mS cm $^{-1}$ with a polymer loading of 12%. The electrochemical performance of the polymer composite electrolyte is tested by the Li stripping-plating test, and the results show that it has better cyclic stability (>100 cycles) than that of the pristine LiPS material.

In addition, a polymer grafting method is employed to chemically attach a self-healable functional monomer (ureidopyrimidinone methacrylate; UrP) over the surface of Li_{3.85}Sn_{0.85}Sb_{0.15}S₄ (LiSnSbS) solid electrolyte [187]. The monomer-grafted LiSnSbS electrolyte is evenly distributed in the poly(styrene-butadiene-styrene)-based elastomeric matrix (Figure 10e). The self-healable UrP group is also attached to the elastomeric chains, which boosts the self-repair of any cracks that occur during the life cycle of the assembled device through the strong hydrogen-bonding interactions among the UrP units (Figure 10f). The fabricated LIB (LiNi_{0.9}Mn_{0.05}Co_{0.05}O₂ as a cathode) composed of the LiSnSbS-polymer composite electrolyte exhibits a capacity retention of 82% after 140 GCD cycles. The device is further tested under controlled pressure of 160 kPa for more than 140 GCD cycles at a 0.5 C rate. Even under applied pressure, the device possesses $>92\%$ of its capacity when compared to that without applied pressure. The improved electrochemical performance is attributed to the following factors: (i) The self-healable composite electrolyte effectively prevents the formation of dendritic growth at interphase, and (ii) any change in the volume of the electrode during the charge-discharge process is easily managed by the elastomeric composite matrix. Moreover, there is still scope to enhance the ionic conductivity of these solid electrolytes by tuning the particle size, weight percentage, and homogeneous distribution of fillers. The better electrochemical performances of the composite electrolytes result from the synergistic effect on Li⁺ ion transport properties of the evenly distributed ceramic fillers in the polymer matrix with a maximum accessible surface area. In the composite electrolytes, the poor electrode-electrolyte interfacial contact could be overcome by incorporating a soft glue/adhesive layer between the electrode and composite electrolytes. For example, a composite cellulose acetate/polyethyleneglycol/LATP layer with an ionic liquid on the side of the composite electrolyte solved the issue associated with inferior physical contact and higher interfacial impedance [188]. Similarly, LiTFSI/dimethoxyethane

is applied over both sides of the Li_3PS_4 -based composite electrolyte to minimize interfacial impedance and also lithium dendrite formation [189].

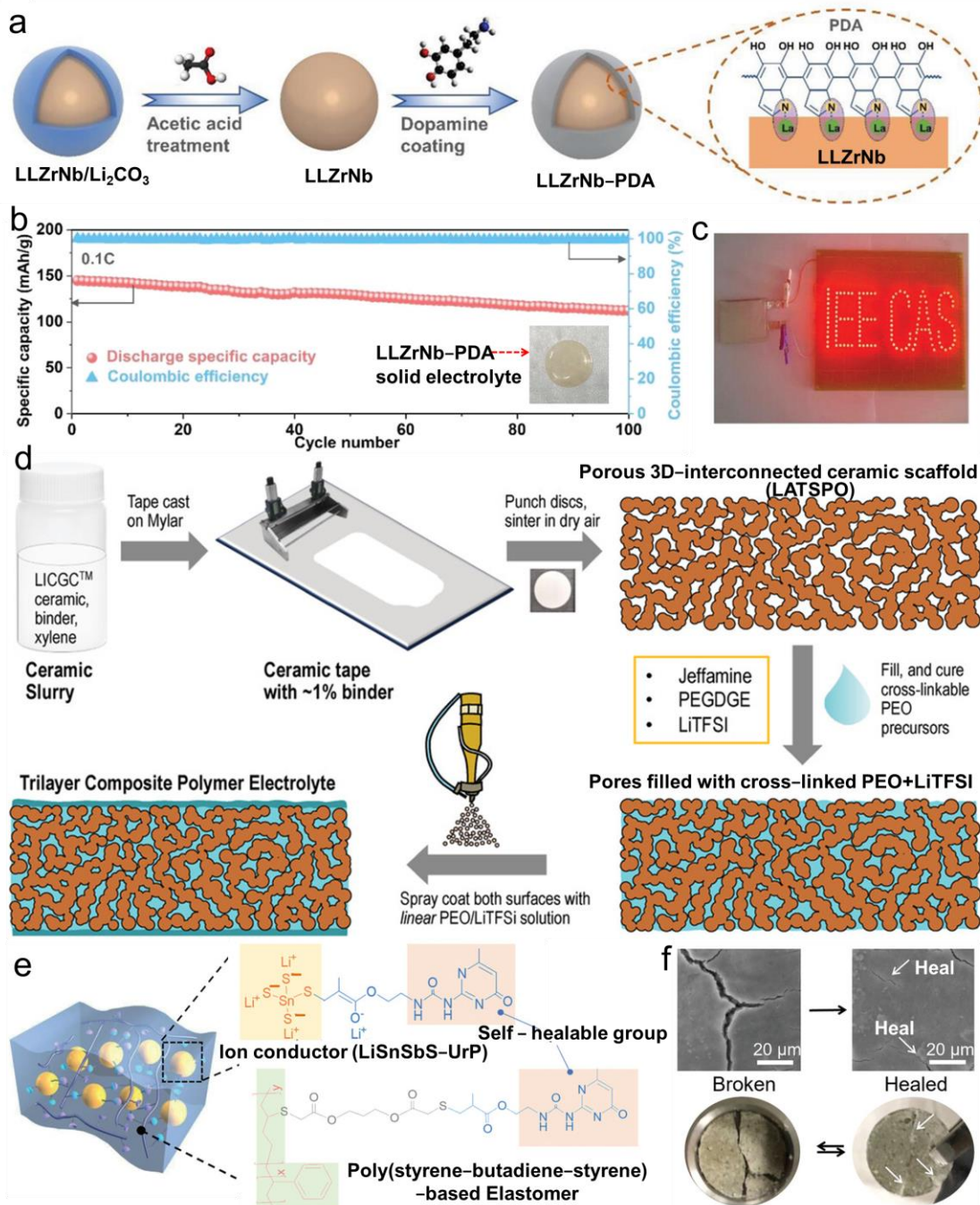


Figure 10. (a) Preparation of $\text{Li}_{6.4}\text{La}_3\text{Zr}_{1.4}\text{Nb}_{0.6}\text{O}_{12}$ (LLZrNb)-PDA polymer composite electrolyte [121]. (b) A plot of specific capacity vs. number of cycles of LIB assembled with the LLZrNb-PDA composite electrolyte; and (c) a photograph showing the lighting-up of 140 LED bulbs with the fully charged LIB with the LLZrNb-PDA composite electrolyte. (d) Preparation of a trilayer structure of $\text{Li}_{1+x+y}\text{Al}_x\text{Ti}_{2-x}\text{Si}_y\text{P}_3-y\text{O}_{12}$ (LATSCO)/cross-linkable polyethyleneoxide (PEO)/LiTFSI polymer composite electrolyte [185]. (e) Schematic representation showing the design of a self-healable ureidopyrimidinone methacrylate (UrP)-grafted $\text{Li}_{3.85}\text{Sn}_{0.85}\text{Sb}_{0.15}\text{S}_4$ (LiSnSbS) solid electrolyte within the poly(styrene-butadiene-styrene)-based elastomeric matrix [187]. (f) Photographs showing the self-healing behavior of the LiSnSbS polymer composite electrolyte film.

4. Summary and Outlook

Polymeric composites comprising various polymers and inorganic compounds/nanocrystals/carbon nanomaterials are examined with a focus on high-performance energy conversion (solar cells, photocatalytic hydrogen production, and nanogenerators) and storage (supercapacitors and metal-ion batteries) devices via very recent representative examples. Composing the conducting polymers (PANI, PEDOT, PPy, and PTH)/non-conducting polymers (PVDF, PVA, and PMMA) with inorganic compounds (TiO_2 , ZnO , CdSe, and PbBr_3) and carbon nanomaterials (carbon nanotubes, graphene, and carbon nanofibers) significantly improves the mechanical, thermal, and electronic properties with tuned interfacial characteristics. The introduction of molecular-level interactions between the polymers and other components of the composite materials through a covalent or noncovalent approach is crucial to enhancing the interfacial properties such as surface adhesion, wettability, domain morphology, and interfacial charge transfer, which are essential for high-performance energy materials. Though vast varieties of polymeric composites have been developed recently, their performances in energy conversion and storage devices still need major improvements to fulfill the huge demand for high-performance functional materials for advanced futuristic applications.

To achieve optimal interfacial characteristics, an in-depth understanding of the mechanisms of interfacial processes is necessary to investigate and further modify synthetic and device fabrication techniques. The various interactions, namely, physical attraction (among electrically neutral components), electrostatic, and covalent bonding, together with the weak interactions such as hydrogen bonding and van der Waals forces, control largely the interfacial properties. The types of interactions operating in a given polymeric composite material depend on the molecular as well as structural properties of the individual components. The structural-tuning approach is the most preferable technique to achieve high-performance energy materials. For instance, a high concentration of active heterojunctions could be obtained from the structurally tuned polymers, thereby enhancing the charge separation/transfer kinetics at the interfaces. Integrated and more accurate characterization techniques, such as *in-situ* spectroscopic and microscopic methods, are necessary to further improve the interfacial properties that control the device's performance. Moreover, computational techniques need to be employed extensively to characterize the interfacial properties to greatly reduce the manpower and synthetic cost involved in the experimental screening of new composite materials. For example, the molecular dynamics methods could provide an idea about the optimal polymeric structures with appropriate chemical groups for high-performance materials by stimulating the interfacial interactions among the components.

In addition to the structural and property tuning methods, the device fabrication techniques also need rigorous advancements to effectively employ the optimized polymer composites for higher performance. In this context, the three-dimensional (3D) printing technique could furnish several advantages in the construction of device constituents with preferred geometry and their assembly with high accuracy. Further, the 3D printing method offers various advanced methodologies, such as fused deposition, inkjet, and stereolithography, to handle different types of composite materials. These methods also enable us to control the composition of materials in the different building parts of the fabricated device constituents. Extensive research in the development of high-performance polymeric materials with the effective utilization of synthetic as well as computational methods, together with unprecedented device fabrications, would pave a path towards futuristic advanced energy devices.

Author Contributions: B.V. and K.C.S.L. contributed equally. B.V.: Conceptualization, Methodology, Validation, Investigation, Data Curation, Writing—Reviewing and Editing, Visualization, Supervision. K.C.S.L.: Conceptualization, Methodology, Investigation, Data Curation, Writing—Reviewing and Editing, Visualization. T.-W.L.: Conceptualization, Methodology, Validation, Writing—Reviewing and Editing, Visualization. All authors have read and agreed to the published version of the manuscript.

Funding: This research received no external funding.

Data Availability Statement: Some figures in this review are reproduced from previously published articles. However, the proper copyright permissions were obtained through “CCC Rightslink”. Figure 2c (Permission was granted by the American Chemical Society, a licence number was not generated from the system, 20 June 2023); Figure 2d-Licence 5573620478601, 21 June 2023; Figure 2e (Permission was granted by the American Chemical Society, a licence number was not generated from the system, 21 June 2023); Figure 3a-Licence 5572630110032, 21 June 2023; Figure 3b–d-Licence 557363795927, 21 June 2023; Figure 3e-Licence 5573640452132, 21 June 2023; Figure 3f-Licence 1367857-1, 22 June 2023; Figure 4a-Licence 5573940814147, 21 June 2023; Figure 4b,c (Permission was granted by the American Chemical Society, a licence number was not generated from the system, 22 June 2023); Figure 4d,e-Licence 5573950064460, 21 June 2023; Figure 5a,b-Licence 5573950953002, 21 June 2023; Figure 5c-Licence 5573961507199, 21 June 2023); Figure 5d-Licence 5573970853523, 21 June 2023); Figure 5e-Licence 5573990311755, 21 June 2023); Figure 6a–c (Permission under Creative Commons License-CC BY 4.0); Figure 6d-Licence 5574111493404, 22 June 2023); Figure 7a-Licence 5574120230839, 22 June 2023); Figure 7b-Licence 5574120437656, 22 June 2023); Figure 7c (Permission was granted by the American Chemical Society, a licence number was not generated from the system, 22 June 2023); Figure 8a-Licence 1367935-1, 22 June 2023); Figure 8b (Permission was granted by the American Chemical Society, a licence number was not generated from the system, 22 June 2023); Figure 8c,d-Licence 5574130368974, 22 June 2023); Figure 9a,b-Licence 1367941-1, 22 June 2023); Figure 9c,d (Permission was granted by the American Chemical Society, a licence number was not generated from the system, 22 June 2023); Figure 10a–c-Licence 5574131294393, 22 June 2023); Figure 10d-Licence 5574140068986, 22 June 2023); Figure 10e,f-Licence 5574140302644, 22 June 2023).

Acknowledgments: B.V. acknowledges the ‘Japan Society for the Promotion of Science’ for a research fellowship (P21035). K.C.S.L. acknowledges ‘Chiba University’, Japan, for a research fellowship.

Conflicts of Interest: The authors declare no conflict of interest.

References

1. Ellabban, O.; Abu-Rub, H.; Blaabjerg, F. Renewable energy resources: Current status, future prospects and their enabling technology. *Renew. Sustain. Energy Rev.* **2014**, *39*, 748–764. [[CrossRef](#)]
2. Hoffert, M.I.; Caldeira, K.; Benford, G.; Criswell, D.R.; Green, C.; Herzog, H.; Jain, A.K.; Kheshgi, H.S.; Lackner, K.S.; Lewis, J.S.; et al. Advanced Technology Paths to Global Climate Stability: Energy for a Greenhouse Planet. *Science* **2002**, *298*, 981–987. [[CrossRef](#)]
3. Seferlis, P.; Varbanov, P.S.; Papadopoulos, A.I.; Chin, H.H.; Klemeš, J.J. Sustainable design, integration, and operation for energy high-performance process systems. *Energy* **2021**, *224*, 120158. [[CrossRef](#)]
4. Luo, H.; Barrio, J.; Sunny, N.; Li, A.; Steier, L.; Shah, N.; Stephens, I.E.L.; Titirici, M.-M. Progress and Perspectives in Photo- and Electrochemical-Oxidation of Biomass for Sustainable Chemicals and Hydrogen Production. *Adv. Energy Mater.* **2021**, *11*, 2101180. [[CrossRef](#)]
5. Bairagi, S.; Shahid ul, I.; Shahadat, M.; Mulvihill, D.M.; Ali, W. Mechanical energy harvesting and self-powered electronic applications of textile-based piezoelectric nanogenerators: A systematic review. *Nano Energy* **2023**, *111*, 108414. [[CrossRef](#)]
6. Obaideen, K.; Olabi, A.G.; Al Swailmeen, Y.; Shehata, N.; Abdelkareem, M.A.; Alami, A.H.; Rodriguez, C.; Sayed, E.T. Solar Energy: Applications, Trends Analysis, Bibliometric Analysis and Research Contribution to Sustainable Development Goals (SDGs). *Sustainability* **2023**, *15*, 1418. [[CrossRef](#)]
7. Ashraf, M.; Ayaz, M.; Khan, M.; Adil, S.F.; Farooq, W.; Ullah, N.; Nawaz Tahir, M. Recent Trends in Sustainable Solar Energy Conversion Technologies: Mechanisms, Prospects, and Challenges. *Energy Fuels* **2023**, *37*, 6283–6301. [[CrossRef](#)]
8. Xie, Y.; Lu, H.; Huang, J.; Xie, H. Natural Materials for Sustainable Organic Solar Cells: Status and Challenge. *Adv. Funct. Mater.* **2023**, *33*, 2213910. [[CrossRef](#)]
9. Liu, Y.; Tan, X.; Liang, J.; Han, H.; Xiang, P.; Yan, W. Machine Learning for Perovskite Solar Cells and Component Materials: Key Technologies and Prospects. *Adv. Funct. Mater.* **2023**, *33*, 2214271. [[CrossRef](#)]
10. Brabec, C.J.; Gowrisanker, S.; Halls, J.J.M.; Laird, D.; Jia, S.; Williams, S.P. Polymer–Fullerene Bulk-Heterojunction Solar Cells. *Adv. Mater.* **2010**, *22*, 3839–3856. [[CrossRef](#)]
11. Lee, J.-W.; Cho, K.-H.; Yoon, J.-S.; Kim, Y.-M.; Sung, Y.-M. Photoelectrochemical water splitting using one-dimensional nanostructures. *J. Mater. Chem. A* **2021**, *9*, 21576–21606. [[CrossRef](#)]
12. Chatenet, M.; Pollet, B.G.; Dekel, D.R.; Dionigi, F.; Deseure, J.; Millet, P.; Braatz, R.D.; Bazant, M.Z.; Eikerling, M.; Staffell, I.; et al. Water electrolysis: From textbook knowledge to the latest scientific strategies and industrial developments. *Chem. Soc. Rev.* **2022**, *51*, 4583–4762. [[CrossRef](#)] [[PubMed](#)]
13. Song, H.; Luo, S.; Huang, H.; Deng, B.; Ye, J. Solar-Driven Hydrogen Production: Recent Advances, Challenges, and Future Perspectives. *ACS Energy Lett.* **2022**, *7*, 1043–1065. [[CrossRef](#)]

14. Nikolaidis, P.; Poulikkas, A. A comparative overview of hydrogen production processes. *Renew. Sustain. Energy Rev.* **2017**, *67*, 597–611. [[CrossRef](#)]
15. Zhang, D.; Wang, Y.; Yang, Y. Design, Performance, and Application of Thermoelectric Nanogenerators. *Small* **2019**, *15*, 1805241. [[CrossRef](#)] [[PubMed](#)]
16. Deng, W.; Zhou, Y.; Libanori, A.; Chen, G.; Yang, W.; Chen, J. Piezoelectric nanogenerators for personalized healthcare. *Chem. Soc. Rev.* **2022**, *51*, 3380–3435. [[CrossRef](#)]
17. Khandelwal, G.; Maria Joseph Raj, N.P.; Kim, S.-J. Materials Beyond Conventional Triboelectric Series for Fabrication and Applications of Triboelectric Nanogenerators. *Adv. Energy Mater.* **2021**, *11*, 2101170. [[CrossRef](#)]
18. Lakshmi, K.C.S.; Vedhanarayanan, B. High-Performance Supercapacitors: A Comprehensive Review on Paradigm Shift of Conventional Energy Storage Devices. *Batteries* **2023**, *9*, 202. [[CrossRef](#)]
19. Palacín, M.R. Recent advances in rechargeable battery materials: A chemist's perspective. *Chem. Soc. Rev.* **2009**, *38*, 2565–2575. [[CrossRef](#)]
20. Swain, N.; Tripathy, A.; Thirumurugan, A.; Saravanakumar, B.; Schmidt-Mende, L.; Ramadoss, A. A brief review on stretchable, compressible, and deformable supercapacitor for smart devices. *Chem. Eng. J.* **2022**, *446*, 136876. [[CrossRef](#)]
21. Faber, M.S.; Jin, S. Earth-abundant inorganic electrocatalysts and their nanostructures for energy conversion applications. *Energy Environ. Sci.* **2014**, *7*, 3519–3542. [[CrossRef](#)]
22. Tajik, S.; Beitollahi, H.; Dourandish, Z.; Mohammadzadeh Jahani, P.; Sheikhshoaei, I.; Askari, M.B.; Salarizadeh, P.; Nejad, F.G.; Kim, D.; Kim, S.Y.; et al. Applications of Non-precious Transition Metal Oxide Nanoparticles in Electrochemistry. *Electroanalysis* **2022**, *34*, 1065–1091. [[CrossRef](#)]
23. Wu, H.; Zhuo, F.; Qiao, H.; Kodumudi Venkataraman, L.; Zheng, M.; Wang, S.; Huang, H.; Li, B.; Mao, X.; Zhang, Q. Polymer-/Ceramic-based Dielectric Composites for Energy Storage and Conversion. *Energy Environ. Mater.* **2022**, *5*, 486–514. [[CrossRef](#)]
24. Lakshmi, K.C.S.; Vedhanarayanan, B.; Lin, T.-W. Electrocatalytic hydrogen and oxygen evolution reactions: Role of two-dimensional layered materials and their composites. *Electrochim. Acta* **2023**, *447*, 142119. [[CrossRef](#)]
25. Nikoloudakis, E.; López-Duarte, I.; Charalambidis, G.; Ladomenou, K.; Ince, M.; Coutsolelos, A.G. Porphyrins and phthalocyanines as biomimetic tools for photocatalytic H₂ production and CO₂ reduction. *Chem. Soc. Rev.* **2022**, *51*, 6965–7045. [[CrossRef](#)]
26. Wang, D.-G.; Qiu, T.; Guo, W.; Liang, Z.; Tabassum, H.; Xia, D.; Zou, R. Covalent organic framework-based materials for energy applications. *Energy Environ. Sci.* **2021**, *14*, 688–728. [[CrossRef](#)]
27. Su, X.; Wu, Q.; Li, J.; Xiao, X.; Lott, A.; Lu, W.; Sheldon, B.W.; Wu, J. Silicon-Based Nanomaterials for Lithium-Ion Batteries: A Review. *Adv. Energy Mater.* **2014**, *4*, 1300882. [[CrossRef](#)]
28. Zhang, G.; Finefrock, S.; Liang, D.; Yadav, G.G.; Yang, H.; Fang, H.; Wu, Y. Semiconductor nanostructure-based photovoltaic solar cells. *Nanoscale* **2011**, *3*, 2430–2443. [[CrossRef](#)]
29. Li, B.; Yang, X.; Li, S.; Yuan, J. Stable block copolymer single-material organic solar cells: Progress and perspective. *Energy Environ. Sci.* **2023**, *16*, 723–744. [[CrossRef](#)]
30. Keru, G.; Ndungu, P.G.; Nyamori, V.O. A review on carbon nanotube/polymer composites for organic solar cells. *Int. J. Energy Res.* **2014**, *38*, 1635–1653. [[CrossRef](#)]
31. Jin, J.; Wang, Q.; Ma, K.; Shen, W.; Belfiore, L.A.; Bao, X.; Tang, J. Recent Developments of Polymer Solar Cells with Photovoltaic Performance over 17%. *Adv. Funct. Mater.* **2023**, *33*, 2213324. [[CrossRef](#)]
32. Xie, C.; Liu, Y.; Wei, W.; Zhou, Y. Large-Area Flexible Organic Solar Cells with a Robust Silver Nanowire-Polymer Composite as Transparent Top Electrode. *Adv. Funct. Mater.* **2023**, *33*, 2210675. [[CrossRef](#)]
33. Bouclé, J.; Ackermann, J. Solid-state dye-sensitized and bulk heterojunction solar cells using TiO₂ and ZnO nanostructures: Recent progress and new concepts at the borderline. *Polym. Int.* **2012**, *61*, 355–373. [[CrossRef](#)]
34. Jao, M.-H.; Liao, H.-C.; Su, W.-F. Achieving a high fill factor for organic solar cells. *J. Mater. Chem. A* **2016**, *4*, 5784–5801. [[CrossRef](#)]
35. Niederhausen, J.; Mazzio, K.A.; MacQueen, R.W. Inorganic–organic interfaces in hybrid solar cells. *Electron. Struct.* **2021**, *3*, 033002. [[CrossRef](#)]
36. Sun, Z.; He, Y.; Xiong, B.; Chen, S.; Li, M.; Zhou, Y.; Zheng, Y.; Sun, K.; Yang, C. Performance-Enhancing Approaches for PEDOT:PSS-Si Hybrid Solar Cells. *Angew. Chem.-Int. Ed.* **2021**, *60*, 5036–5055. [[CrossRef](#)]
37. Oh, H.; Kang, G.; Park, M. Polymer-Mediated In Situ Growth of Perovskite Nanocrystals in Electrospinning: Design of Composite Nanofiber-Based Highly Efficient Luminescent Solar Concentrators. *ACS Appl. Energy Mater.* **2022**, *5*, 15844–15855. [[CrossRef](#)]
38. Beek, W.J.E.; Slooff, L.H.; Wienk, M.M.; Kroon, J.M.; Janssen, R.A.J. Hybrid Solar Cells Using a Zinc Oxide Precursor and a Conjugated Polymer. *Adv. Funct. Mater.* **2005**, *15*, 1703–1707. [[CrossRef](#)]
39. Wang, C.; Hu, Z.-Y.; Zhao, H.; Yu, W.; Wu, S.; Liu, J.; Chen, L.; Li, Y.; Su, B.-L. Probing conducting polymers@cadmium sulfide core-shell nanorods for highly improved photocatalytic hydrogen production. *J. Colloid Interface Sci.* **2018**, *521*, 1–10. [[CrossRef](#)]
40. Chen, B.; Wang, X.; Dong, W.; Zhang, X.; Rao, L.; Chen, H.; Huang, D.; Xiang, Y. Enhanced Light-Driven Hydrogen-Production Activity Induced by Accelerated Interfacial Charge Transfer in Donor–Acceptor Conjugated Polymers/TiO₂ Hybrid. *Chem.-Asian J.* **2019**, *25*, 3362–3368. [[CrossRef](#)]
41. Ryu, S.H.; Kim, G.H.; Ahn, T.K.; Ko, K.C.; Son, S.U. Enhanced photocatalytic hydrogen production of microporous organic polymers by incorporation of afterglow phosphorescent materials. *J. Mater. Chem. A* **2023**, *11*, 12719–12725. [[CrossRef](#)]

42. Chi, C.; An, M.; Qi, X.; Li, Y.; Zhang, R.; Liu, G.; Lin, C.; Huang, H.; Dang, H.; Demir, B.; et al. Selectively tuning ionic thermopower in all-solid-state flexible polymer composites for thermal sensing. *Nat. Commun.* **2022**, *13*, 221. [CrossRef] [PubMed]
43. Hong, Y.; Wang, B.; Long, Z.; Zhang, Z.; Pan, Q.; Liu, S.; Luo, X.; Yang, Z. Hierarchically Interconnected Piezoceramic Textile with a Balanced Performance in Piezoelectricity, Flexibility, Toughness, and Air Permeability. *Adv. Funct. Mater.* **2021**, *31*, 2104737. [CrossRef]
44. Paranjape, M.V.; Graham, S.A.; Manchi, P.; Kurakula, A.; Yu, J.S. Multistage SrBaTiO₃/PDMS Composite Film-Based Hybrid Nanogenerator for Efficient Floor Energy Harvesting Applications. *Small* **2023**, *19*, 2300535. [CrossRef]
45. Kang, H.; Lee, W.; Oh, J.; Kim, T.; Lee, C.; Kim, B.J. From Fullerene–Polymer to All-Polymer Solar Cells: The Importance of Molecular Packing, Orientation, and Morphology Control. *Acc. Chem. Res.* **2016**, *49*, 2424–2434. [CrossRef]
46. Nogueira, A.F.; Durrant, J.R.; De Paoli, M.A. Dye-Sensitized Nanocrystalline Solar Cells Employing a Polymer Electrolyte. *Adv. Mater.* **2001**, *13*, 826–830. [CrossRef]
47. Ravirajan, P.; Peiró, A.M.; Nazeeruddin, M.K.; Graetzel, M.; Bradley, D.D.C.; Durrant, J.R.; Nelson, J. Hybrid Polymer/Zinc Oxide Photovoltaic Devices with Vertically Oriented ZnO Nanorods and an Amphiphilic Molecular Interface Layer. *J. Phys. Chem. B* **2006**, *110*, 7635–7639. [CrossRef] [PubMed]
48. Liu, Y.; Scully, S.R.; McGehee, M.D.; Liu, J.; Luscombe, C.K.; Fréchet, J.M.J.; Shaheen, S.E.; Ginley, D.S. Dependence of Band Offset and Open-Circuit Voltage on the Interfacial Interaction between TiO₂ and Carboxylated Polythiophenes. *J. Phys. Chem. B* **2006**, *110*, 3257–3261. [CrossRef]
49. Chen, Z.; Du, X.; Zeng, Q.; Yang, B. Recent development and understanding of polymer–nanocrystal hybrid solar cells. *Mater. Chem. Front.* **2017**, *1*, 1502–1513. [CrossRef]
50. Huynh, W.U.; Dittmer, J.J.; Alivisatos, A.P. Hybrid Nanorod–Polymer Solar Cells. *Science* **2002**, *295*, 2425–2427. [CrossRef]
51. Sun, B.; Snaith, H.J.; Dhoot, A.S.; Westenhoff, S.; Greenham, N.C. Vertically segregated hybrid blends for photovoltaic devices with improved efficiency. *J. Appl. Phys.* **2005**, *97*, 014914. [CrossRef]
52. Cui, D.; Xu, J.; Zhu, T.; Paradee, G.; Ashok, S.; Gerhold, M. Harvest of near infrared light in PbSe nanocrystal–polymer hybrid photovoltaic cells. *Appl. Phys. Lett.* **2006**, *88*, 183111. [CrossRef]
53. Beek, W.J.E.; Wienk, M.M.; Janssen, R.A.J. Efficient Hybrid Solar Cells from Zinc Oxide Nanoparticles and a Conjugated Polymer. *Adv. Mater.* **2004**, *16*, 1009–1013. [CrossRef]
54. Kwong, C.Y.; Djurišić, A.B.; Chui, P.C.; Cheng, K.W.; Chan, W.K. Influence of solvent on film morphology and device performance of poly(3-hexylthiophene):TiO₂ nanocomposite solar cells. *Chem. Phys. Lett.* **2004**, *384*, 372–375. [CrossRef]
55. Zeng, T.-W.; Lin, Y.-Y.; Lo, H.-H.; Chen, C.-W.; Chen, C.-H.; Liou, S.-C.; Huang, H.-Y.; Su, W.-F. A large interconnecting network within hybrid MEH-PPV/TiO₂nanorod photovoltaic devices. *Nanotechnology* **2006**, *17*, 5387–5392. [CrossRef]
56. Querner, C.; Reiss, P.; Bleuse, J.; Pron, A. Chelating Ligands for Nanocrystals’ Surface Functionalization. *J. Am. Chem. Soc.* **2004**, *126*, 11574–11582. [CrossRef]
57. Huynh, W.U.; Dittmer, J.J.; Libby, W.C.; Whiting, G.L.; Alivisatos, A.P. Controlling the Morphology of Nanocrystal–Polymer Composites for Solar Cells. *Adv. Funct. Mater.* **2003**, *13*, 73–79. [CrossRef]
58. Beek, W.J.E.; Wienk, M.M.; Janssen, R.A.J. Hybrid Solar Cells from Regioregular Polythiophene and ZnO Nanoparticles. *Adv. Funct. Mater.* **2006**, *16*, 1112–1116. [CrossRef]
59. Li, Z.; Fang, S.; Sun, H.; Chung, R.-J.; Fang, X.; He, J.-H. Solar Hydrogen. *Adv. Energy Mater.* **2023**, *13*, 2203019. [CrossRef]
60. Wang, Y.; Chen, K.S.; Mishler, J.; Cho, S.C.; Adroher, X.C. A review of polymer electrolyte membrane fuel cells: Technology, applications, and needs on fundamental research. *Appl. Energy* **2011**, *88*, 981–1007. [CrossRef]
61. Kranz, C.; Wächtler, M. Characterizing photocatalysts for water splitting: From atoms to bulk and from slow to ultrafast processes. *Chem. Soc. Rev.* **2021**, *50*, 1407–1437. [CrossRef] [PubMed]
62. Mansha, M.; Ahmad, T.; Ullah, N.; Akram Khan, S.; Ashraf, M.; Ali, S.; Tan, B.; Khan, I. Photocatalytic Water-Splitting by Organic Conjugated Polymers: Opportunities and Challenges. *Chem. Rec.* **2022**, *22*, e202100336. [CrossRef] [PubMed]
63. Moniz, S.J.A.; Shevlin, S.A.; Martin, D.J.; Guo, Z.-X.; Tang, J. Visible-light driven heterojunction photocatalysts for water splitting—A critical review. *Energy Environ. Sci.* **2015**, *8*, 731–759. [CrossRef]
64. Bon, C.Y.; Mohammed, L.; Kim, S.; Manasi, M.; Isheunesu, P.; Lee, K.S.; Ko, J.M. Flexible poly(vinyl alcohol)-ceramic composite separators for supercapacitor applications. *J. Ind. Eng. Chem.* **2018**, *68*, 173–179. [CrossRef]
65. Xu, S.; Han, Y.; Xu, Y.; Meng, H.; Xu, J.; Wu, J.; Xu, Y.; Zhang, X. Fabrication of polyaniline sensitized grey-TiO₂ nanocomposites and enhanced photocatalytic activity. *Sep. Purif. Technol.* **2017**, *184*, 248–256. [CrossRef]
66. Zielińska, B.; Schmidt, B.; Mijowska, E.; Kaleńczuk, R. PANI/NaTaO composite photocatalyst for enhanced hydrogen generation under UV light irradiation. *Pol. J. Chem. Technol.* **2017**, *19*, 115–119. [CrossRef]
67. Chang, C.-J.; Chu, K.-W. ZnS/polyaniline composites with improved dispersing stability and high photocatalytic hydrogen production activity. *Int. J. Hydrogen Energy* **2016**, *41*, 21764–21773. [CrossRef]
68. Nsib, M.F.; Naffati, N.; Rayes, A.; Moussa, N.; Houas, A. Effect of some operational parameters on the hydrogen generation efficiency of Ni-ZnO/PANI composite under visible-light irradiation. *Mater. Res. Bull.* **2015**, *70*, 530–538. [CrossRef]
69. Sasaki, R.; Gaikwad, A.P.; Jayakumar, O.D.; Girija, K.G.; Rao, R.; Tyagi, A.K.; Bharadwaj, S.R. Nano-hybrid MoS₂-PANI-CdS photocatalyst for hydrogen evolution from water. *Colloid Surf. A-Physicochem. Eng. Asp.* **2015**, *481*, 485–492. [CrossRef]
70. Zhou, W.; Lu, S.; Chen, X. Anionic donor–acceptor conjugated polymer dots/g-C₃N₄ nanosheets heterojunction: High efficiency and excellent stability for co-catalyst-free photocatalytic hydrogen evolution. *J. Colloid Interface Sci.* **2022**, *608*, 912–921. [CrossRef]

71. Li, X.; Wang, P.; Huang, B.; Qin, X.; Zhang, X.; Zhang, Q.; Zhu, X.; Dai, Y. Precisely locate Pd-Polypyrrole on TiO₂ for enhanced hydrogen production. *Int. J. Hydrogen Energy* **2017**, *42*, 25195–25202. [CrossRef]
72. Wang, X.; Feng, S.; Zhao, W.; Zhao, D.; Chen, S. Ag/polyaniline heterostructured nanosheets loaded with g-C3N4 nanoparticles for highly efficient photocatalytic hydrogen generation under visible light. *New J. Chem.* **2017**, *41*, 9354–9360. [CrossRef]
73. Fan, F.R.; Tang, W.; Wang, Z.L. Flexible Nanogenerators for Energy Harvesting and Self-Powered Electronics. *Adv. Mater.* **2016**, *28*, 4283–4305. [CrossRef]
74. Tainoff, D.; Proudhom, A.; Tur, C.; Crozes, T.; Dufresnes, S.; Dumont, S.; Bourgault, D.; Bourgeois, O. Network of thermoelectric nanogenerators for low power energy harvesting. *Nano Energy* **2019**, *57*, 804–810. [CrossRef]
75. Briscoe, J.; Dunn, S. Piezoelectric nanogenerators—A review of nanostructured piezoelectric energy harvesters. *Nano Energy* **2015**, *14*, 15–29. [CrossRef]
76. Du, T.; Dong, F.; Xi, Z.; Zhu, M.; Zou, Y.; Sun, P.; Xu, M. Recent Advances in Mechanical Vibration Energy Harvesters Based on Triboelectric Nanogenerators. *Small* **2023**, *19*, 2300401. [CrossRef]
77. Yoon, H.-J.; Kim, S.-W. Nanogenerators to Power Implantable Medical Systems. *Joule* **2020**, *4*, 1398–1407. [CrossRef]
78. Fiedler, C.; Kleinhanns, T.; Garcia, M.; Lee, S.; Calcabrini, M.; Ibáñez, M. Solution-Processed Inorganic Thermoelectric Materials: Opportunities and Challenges. *Chem. Mater.* **2022**, *34*, 8471–8489. [CrossRef]
79. Cao, Y.Q.; Zhao, X.B.; Zhu, T.J.; Zhang, X.B.; Tu, J.P. Syntheses and thermoelectric properties of Bi₂Te₃/Sb₂Te₃ bulk nanocomposites with laminated nanostructure. *Appl. Phys. Lett.* **2008**, *92*, 143106. [CrossRef]
80. Wang, A.C.; Wu, C.; Pisignano, D.; Wang, Z.L.; Persano, L. Polymer nanogenerators: Opportunities and challenges for large-scale applications. *J. Appl. Polym. Sci.* **2018**, *135*, 45674. [CrossRef]
81. Gao, X.; Uehara, K.; Klug, D.D.; Patchkovskii, S.; Tse, J.S.; Tritt, T.M. Theoretical studies on the thermopower of semiconductors and low-band-gap crystalline polymers. *Phys. Rev. B* **2005**, *72*, 125202. [CrossRef]
82. Schlitz, R.A.; Brunetti, F.G.; Glaudell, A.M.; Miller, P.L.; Brady, M.A.; Takacs, C.J.; Hawker, C.J.; Chabinyc, M.L. Solubility-Limited Extrinsic n-Type Doping of a High Electron Mobility Polymer for Thermoelectric Applications. *Adv. Mater.* **2014**, *26*, 2825–2830. [CrossRef] [PubMed]
83. Wang, Y.; Cai, K.; Yao, X. Facile Fabrication and Thermoelectric Properties of PbTe-Modified Poly(3,4-ethylenedioxythiophene) Nanotubes. *ACS Appl. Mater. Interfaces* **2011**, *3*, 1163–1166. [CrossRef] [PubMed]
84. Li, Z.; Deng, L.; Lv, H.; Liang, L.; Deng, W.; Zhang, Y.; Chen, G. Mechanically Robust and Flexible Films of Ionic Liquid-Modulated Polymer Thermoelectric Composites. *Adv. Funct. Mater.* **2021**, *31*, 2104836. [CrossRef]
85. Liu, C.; Yin, X.; Chen, Z.; Gao, C.; Wang, L. Improving the thermoelectric performance of solution-processed polymer nanocomposites by introducing platinum acetylides with tailored intermolecular interactions. *Chem. Eng. J.* **2021**, *419*, 129624. [CrossRef]
86. McGrail, B.T.; Sehirlioglu, A.; Pentzer, E. Polymer Composites for Thermoelectric Applications. *Angew. Chem.-Int. Ed.* **2015**, *54*, 1710–1723. [CrossRef]
87. Chen, W.; Zheng, Q.; Lv, Y.A.; Chen, Y.; Fan, Q.; Zhou, X.; Li, H.; Yu, Q.; Liu, H. Piezoelectric energy harvesting and dissipating behaviors of polymer-based piezoelectric composites for nanogenerators and dampers. *Chem. Eng. J.* **2023**, *465*, 142755. [CrossRef]
88. Greeshma, T.; Balaji, R.; Jayakumar, S. PVDF Phase Formation and Its Influence on Electrical and Structural Properties of PZT-PVDF Composites. *Ferroelectr. Lett. Sect.* **2013**, *40*, 41–55. [CrossRef]
89. Hou, Y.; Deng, Y.; Wang, Y.; Gao, H. Uniform distribution of low content BaTiO₃ nanoparticles in poly(vinylidene fluoride) nanocomposite: Toward high dielectric breakdown strength and energy storage density. *RSC Adv.* **2015**, *5*, 72090–72098. [CrossRef]
90. Su, Y.; Li, W.; Yuan, L.; Chen, C.; Pan, H.; Xie, G.; Conta, G.; Ferrier, S.; Zhao, X.; Chen, G.; et al. Piezoelectric fiber composites with polydopamine interfacial layer for self-powered wearable biomonitoring. *Nano Energy* **2021**, *89*, 106321. [CrossRef]
91. Li, R.; Zhao, Z.; Chen, Z.; Pei, J. Novel BaTiO₃/PVDF composites with enhanced electrical properties modified by calcined BaTiO₃ ceramic powders. *Mater. Express* **2017**, *7*, 536–540. [CrossRef]
92. Dodds, J.S.; Meyers, F.N.; Loh, K.J. Piezoelectric Characterization of PVDF-TrFE Thin Films Enhanced with ZnO Nanoparticles. *IEEE Sens. J.* **2012**, *12*, 1889–1890. [CrossRef]
93. Yang, L.; Ji, H.; Zhu, K.; Wang, J.; Qiu, J. Dramatically improved piezoelectric properties of poly(vinylidene fluoride) composites by incorporating aligned TiO₂@MWCNTs. *Compos. Sci. Technol.* **2016**, *123*, 259–267. [CrossRef]
94. Liu, Y.; Ping, J.; Ying, Y. Recent Progress in 2D-Nanomaterial-Based Triboelectric Nanogenerators. *Adv. Funct. Mater.* **2021**, *31*, 2009994. [CrossRef]
95. Dassanayaka, D.G.; Alves, T.M.; Wanasekara, N.D.; Dharmasena, I.G.; Ventura, J. Recent Progresses in Wearable Triboelectric Nanogenerators. *Adv. Funct. Mater.* **2022**, *32*, 2205438. [CrossRef]
96. He, H.; Guo, J.; Illés, B.; Géczy, A.; Istók, B.; Hliva, V.; Török, D.; Kovács, J.G.; Harmati, I.; Molnár, K. Monitoring multi-respiratory indices via a smart nanofibrous mask filter based on a triboelectric nanogenerator. *Nano Energy* **2021**, *89*, 106418. [CrossRef]
97. Kim, M.P.; Ahn, C.W.; Lee, Y.; Kim, K.; Park, J.; Ko, H. Interfacial polarization-induced high-k polymer dielectric film for high-performance triboelectric devices. *Nano Energy* **2021**, *82*, 105697. [CrossRef]
98. Shin, S.-H.; Kwon, Y.H.; Kim, Y.-H.; Jung, J.-Y.; Lee, M.H.; Nah, J. Triboelectric Charging Sequence Induced by Surface Functionalization as a Method To Fabricate High Performance Triboelectric Generators. *ACS Nano* **2015**, *9*, 4621–4627. [CrossRef]
99. Yu, Y.; Li, Z.; Wang, Y.; Gong, S.; Wang, X. Sequential Infiltration Synthesis of Doped Polymer Films with Tunable Electrical Properties for Efficient Triboelectric Nanogenerator Development. *Adv. Mater.* **2015**, *27*, 4938–4944. [CrossRef]

100. Appamato, I.; Bunriw, W.; Harnchana, V.; Siriwong, C.; Mongkolthanaruk, W.; Thongbai, P.; Chanthat, C.; Chompoosor, A.; Ruangchai, S.; Prada, T.; et al. Engineering Triboelectric Charge in Natural Rubber–Ag Nanocomposite for Enhancing Electrical Output of a Triboelectric Nanogenerator. *ACS Appl. Mater. Interfaces* **2023**, *15*, 973–983. [[CrossRef](#)]
101. Fu, K.; Zhou, J.; Wu, H.; Su, Z. Fibrous self-powered sensor with high stretchability for physiological information monitoring. *Nano Energy* **2021**, *88*, 106258. [[CrossRef](#)]
102. Yang, H.J.; Lee, J.-W.; Seo, S.H.; Jeong, B.; Lee, B.; Do, W.J.; Kim, J.H.; Cho, J.Y.; Jo, A.; Jeong, H.J.; et al. Fully stretchable self-charging power unit with micro-supercapacitor and triboelectric nanogenerator based on oxidized single-walled carbon nanotube/polymer electrodes. *Nano Energy* **2021**, *86*, 106083. [[CrossRef](#)]
103. Wu, C.; Kim, T.W.; Choi, H.Y. Reduced graphene-oxide acting as electron-trapping sites in the friction layer for giant triboelectric enhancement. *Nano Energy* **2017**, *32*, 542–550. [[CrossRef](#)]
104. Wu, C.; Kim, T.W.; Park, J.H.; An, H.; Shao, J.; Chen, X.; Wang, Z.L. Enhanced Triboelectric Nanogenerators Based on MoS₂ Monolayer Nanocomposites Acting as Electron-Acceptor Layers. *ACS Nano* **2017**, *11*, 8356–8363. [[CrossRef](#)] [[PubMed](#)]
105. Cai, X.; Sun, K.; Qiu, Y.; Jiao, X. Recent Advances in Graphene and Conductive Polymer Composites for Supercapacitor Electrodes: A Review. *Crystals* **2021**, *11*, 947. [[CrossRef](#)]
106. Kim, J.-H.; Sharma, A.K.; Lee, Y.-S. Synthesis of polypyrrole and carbon nano-fiber composite for the electrode of electrochemical capacitors. *Mater. Lett.* **2006**, *60*, 1697–1701. [[CrossRef](#)]
107. Kim, J.-H.; Lee, Y.-S.; Sharma, A.K.; Liu, C.G. Polypyrrole/carbon composite electrode for high-power electrochemical capacitors. *Electrochim. Acta* **2006**, *52*, 1727–1732. [[CrossRef](#)]
108. Gupta, V.; Miura, N. Influence of the microstructure on the supercapacitive behavior of polyaniline/single-wall carbon nanotube composites. *J. Power Sources* **2006**, *157*, 616–620. [[CrossRef](#)]
109. Ingram, M.D.; Pappin, A.J.; Delalande, F.; Poupart, D.; Terzulli, G. Development of electrochemical capacitors incorporating processable polymer gel electrolytes. *Electrochim. Acta* **1998**, *43*, 1601–1605. [[CrossRef](#)]
110. Lota, K.; Khomenko, V.; Frackowiak, E. Capacitance properties of poly(3,4-ethylenedioxythiophene)/carbon nanotubes composites. *J. Phys. Chem. Solids* **2004**, *65*, 295–301. [[CrossRef](#)]
111. Frackowiak, E.; Jurewicz, K.; Delpueux, S.; Béguin, F. Nanotubular materials for supercapacitors. *J. Power Sources* **2001**, *97–98*, 822–825. [[CrossRef](#)]
112. Frackowiak, E.; Khomenko, V.; Jurewicz, K.; Lota, K.; Béguin, F. Supercapacitors based on conducting polymers/nanotubes composites. *J. Power Sources* **2006**, *153*, 413–418. [[CrossRef](#)]
113. Choi, J.H.; Noh, J.H.; Choi, C. Highly Elastically Deformable Coiled CNT/Polymer Fibers for Wearable Strain Sensors and Stretchable Supercapacitors. *Sensors* **2023**, *23*, 2359. [[CrossRef](#)] [[PubMed](#)]
114. Tang, S.; Ma, M.; Zhang, X.; Zhao, X.; Fan, J.; Zhu, P.; Shi, K.; Zhou, J. Covalent Cross-Links Enable the Formation of Ambient-Dried Biomass Aerogels through the Activation of a Triazine Derivative for Energy Storage and Generation. *Adv. Funct. Mater.* **2022**, *32*, 2205417. [[CrossRef](#)]
115. Wen, M.; Yu, X.; Yang, C.; Qiu, J.; Zang, L. Compressible zinc-ion hybrid supercapacitor and piezoresistive sensor based on reduced graphene oxide/polypyrrole modified melamine sponge. *Polym. Compos.* **2023**, *44*, 3843–3855. [[CrossRef](#)]
116. Chen, Y.; Liu, X.; Lao, Z.; Yang, K.; Li, F.; Chen, L.; Mai, K.; Zhang, Z. Developing a three-dimensional co-continuous phase network structure via enhanced inter-component affinity for high-performance flexible organic radical electrodes. *J. Mater. Chem. A* **2022**, *10*, 13286–13297. [[CrossRef](#)]
117. Jiang, C.; Zhang, H.; Li, P.; Zhan, X.; Liu, Z.; Wang, L.; Mao, B.; Li, Q.; Wen, Z.; Peng, Z.; et al. A Highly Stable All-Solid-State Na–O₂/H₂O Battery with Low Overpotential Based on Sodium Hydroxide. *Adv. Funct. Mater.* **2022**, *32*, 2202518. [[CrossRef](#)]
118. Li, S.; Wei, X.; Wu, C.; Zhang, B.; Wu, S.; Lin, Z. Constructing Three-Dimensional Structured V₂O₅/Conductive Polymer Composite with Fast Ion/Electron Transfer Kinetics for Aqueous Zinc-Ion Battery. *ACS Appl. Energy Mater.* **2021**, *4*, 4208–4216. [[CrossRef](#)]
119. Nandakumar, D.K.; Vaghasiya, J.V.; Suresh, L.; Duong, T.N.; Tan, S.C. Organic ionic conductors infused aqueous inverse-melting electrolyte aiding crack recovery in flexible supercapacitors functional down to –30 °C. *Mater. Today Energy* **2020**, *17*, 100428. [[CrossRef](#)]
120. Zheng, S.; Chen, Y.; Chen, K.; Yang, S.; Bagherzadeh, R.; Miao, Y.-E.; Liu, T. In situ construction of polyether-based composite electrolyte with bi-phase ion conductivity and stable electrolyte/electrode interphase for solid-state lithium metal batteries. *J. Mater. Chem. A* **2022**, *10*, 19641–19648. [[CrossRef](#)]
121. Xu, Y.; Wang, K.; Zhang, X.; Ma, Y.; Peng, Q.; Gong, Y.; Yi, S.; Guo, H.; Zhang, X.; Sun, X.; et al. Improved Li-Ion Conduction and (Electro)Chemical Stability at Garnet-Polymer Interface through Metal-Nitrogen Bonding. *Adv. Energy Mater.* **2023**, *13*, 2204377. [[CrossRef](#)]
122. Marchionni, F.; Yang, J.; Walker, W.; Wudl, F. A Low Band Gap Conjugated Polymer for Supercapacitor Devices. *J. Phys. Chem. B* **2006**, *110*, 22202–22206. [[CrossRef](#)] [[PubMed](#)]
123. Liu, A.; Li, C.; Bai, H.; Shi, G. Electrochemical Deposition of Polypyrrole/Sulfonated Graphene Composite Films. *J. Phys. Chem. C* **2010**, *114*, 22783–22789. [[CrossRef](#)]
124. Feng, X.; Li, R.; Yan, Z.; Liu, X.; Chen, R.; Ma, Y.; Li, X.; Fan, Q.; Huang, W. Preparation of Graphene/Polypyrrole Composite Film via Electrodeposition for Supercapacitors. *IEEE Trans. Nanotechnol.* **2012**, *11*, 1080–1086. [[CrossRef](#)]

125. Bose, S.; Kim, N.H.; Kuila, T.; Lau, K.-t.; Lee, J.H. Electrochemical performance of a graphene–polypyrrole nanocomposite as a supercapacitor electrode. *Nanotechnology* **2011**, *22*, 295202. [CrossRef]
126. Mini, P.A.; Balakrishnan, A.; Nair, S.V.; Subramanian, K.R.V. Highly super capacitive electrodes made of graphene/poly(pyrrole). *Chem. Commun.* **2011**, *47*, 5753–5755. [CrossRef]
127. Vedhanarayanan, B.; Huang, T.-H.; Lin, T.-W. Fabrication of 3D hierarchically structured carbon electrode for supercapacitors by carbonization of polyaniline/carbon nanotube/graphene composites. *Inorganica Chim. Acta* **2019**, *489*, 217–223. [CrossRef]
128. Cao, H.; Zhou, X.; Zhang, Y.; Chen, L.; Liu, Z. Microspherical polyaniline/graphene nanocomposites for high performance supercapacitors. *J. Power Sources* **2013**, *243*, 715–720. [CrossRef]
129. Hu, N.; Zhang, L.; Yang, C.; Zhao, J.; Yang, Z.; Wei, H.; Liao, H.; Feng, Z.; Fisher, A.; Zhang, Y.; et al. Three-dimensional skeleton networks of graphene wrapped polyaniline nanofibers: An excellent structure for high-performance flexible solid-state supercapacitors. *Sci. Rep.* **2016**, *6*, 19777. [CrossRef]
130. Xu, T.; Yang, D.; Zhang, S.; Zhao, T.; Zhang, M.; Yu, Z.-Z. Antifreezing and stretchable all-gel-state supercapacitor with enhanced capacitances established by graphene/PEDOT-polyvinyl alcohol hydrogel fibers with dual networks. *Carbon* **2021**, *171*, 201–210. [CrossRef]
131. Jellett, C.; Ghosh, K.; Browne, M.P.; Urbanová, V.; Pumera, M. Flexible Graphite–Poly(Lactic Acid) Composite Films as Large-Area Conductive Electrodes for Energy Applications. *ACS Appl. Energy Mater.* **2021**, *4*, 6975–6981. [CrossRef]
132. Yang, J.; Liu, Y.; Liu, S.; Li, L.; Zhang, C.; Liu, T. Conducting polymer composites: Material synthesis and applications in electrochemical capacitive energy storage. *Mater. Chem. Front.* **2017**, *1*, 251–268. [CrossRef]
133. Zang, J.; Bao, S.-J.; Li, C.M.; Bian, H.; Cui, X.; Bao, Q.; Sun, C.Q.; Guo, J.; Lian, K. Well-Aligned Cone-Shaped Nanostructure of Polypyrrole/RuO₂ and Its Electrochemical Supercapacitor. *J. Phys. Chem. C* **2008**, *112*, 14843–14847. [CrossRef]
134. Sharma, R.K.; Rastogi, A.C.; Desu, S.B. Manganese oxide embedded polypyrrole nanocomposites for electrochemical supercapacitor. *Electrochim. Acta* **2008**, *53*, 7690–7695. [CrossRef]
135. Zhang, X.; Ji, L.; Zhang, S.; Yang, W. Synthesis of a novel polyaniline-intercalated layered manganese oxide nanocomposite as electrode material for electrochemical capacitor. *J. Power Sources* **2007**, *173*, 1017–1023. [CrossRef]
136. Liu, R.; Lee, S.B. MnO₂/Poly(3,4-ethylenedioxythiophene) Coaxial Nanowires by One-Step Coelectrodeposition for Electrochemical Energy Storage. *J. Am. Chem. Soc.* **2008**, *130*, 2942–2943. [CrossRef]
137. Sun, B.; He, X.; Leng, X.; Jiang, Y.; Zhao, Y.; Suo, H.; Zhao, C. Flower-like polyaniline–NiO structures: A high specific capacity supercapacitor electrode material with remarkable cycling stability. *RSC Adv.* **2016**, *6*, 43959–43963. [CrossRef]
138. Yang, H.; Xu, H.; Li, M.; Zhang, L.; Huang, Y.; Hu, X. Assembly of NiO/Ni(OH)₂/PEDOT Nanocomposites on Contra Wires for Fiber-Shaped Flexible Asymmetric Supercapacitors. *ACS Appl. Mater. Interfaces* **2016**, *8*, 1774–1779. [CrossRef]
139. Bai, M.-H.; Bian, L.-J.; Song, Y.; Liu, X.-X. Electrochemical Codeposition of Vanadium Oxide and Polypyrrole for High-Performance Supercapacitor with High Working Voltage. *ACS Appl. Mater. Interfaces* **2014**, *6*, 12656–12664. [CrossRef]
140. Lu, X.-F.; Chen, X.-Y.; Zhou, W.; Tong, Y.-X.; Li, G.-R. α -Fe₂O₃@PANI Core–Shell Nanowire Arrays as Negative Electrodes for Asymmetric Supercapacitors. *ACS Appl. Mater. Interfaces* **2015**, *7*, 14843–14850. [CrossRef]
141. Kong, D.; Ren, W.; Cheng, C.; Wang, Y.; Huang, Z.; Yang, H.Y. Three-Dimensional NiCo₂O₄@Polypyrrole Coaxial Nanowire Arrays on Carbon Textiles for High-Performance Flexible Asymmetric Solid-State Supercapacitor. *ACS Appl. Mater. Interfaces* **2015**, *7*, 21334–21346. [CrossRef]
142. Peng, H.; Ma, G.; Sun, K.; Mu, J.; Wang, H.; Lei, Z. High-performance supercapacitor based on multi-structural CuS@polypyrrole composites prepared by in situ oxidative polymerization. *J. Mater. Chem. A* **2014**, *2*, 3303–3307. [CrossRef]
143. Peng, S.; Fan, L.; Wei, C.; Bao, H.; Zhang, H.; Xu, W.; Xu, J. Polypyrrole/nickel sulfide/bacterial cellulose nanofibrous composite membranes for flexible supercapacitor electrodes. *Cellulose* **2016**, *23*, 2639–2651. [CrossRef]
144. Sajedi-Moghaddam, A.; Saievar-Iranizad, E.; Pumera, M. Two-dimensional transition metal dichalcogenide/conducting polymer composites: Synthesis and applications. *Nanoscale* **2017**, *9*, 8052–8065. [CrossRef] [PubMed]
145. Zhu, J.; Sun, W.; Yang, D.; Zhang, Y.; Hoon, H.H.; Zhang, H.; Yan, Q. Multifunctional Architectures Constructing of PANI Nanoneedle Arrays on MoS₂ Thin Nanosheets for High-Energy Supercapacitors. *Small* **2015**, *11*, 4123–4129. [CrossRef] [PubMed]
146. Tang, H.; Wang, J.; Yin, H.; Zhao, H.; Wang, D.; Tang, Z. Growth of Polypyrrole Ultrathin Films on MoS₂ Monolayers as High-Performance Supercapacitor Electrodes. *Adv. Mater.* **2015**, *27*, 1117–1123. [CrossRef]
147. Thiagarajan, K.; Song, W.-J.; Park, H.; Selvaraj, V.; Moon, S.; Oh, J.; Kwak, M.-J.; Park, G.; Kong, M.; Pal, M.; et al. Electroactive 1T-MoS₂ Fluoroelastomer Ink for Intrinsically Stretchable Solid-State In-Plane Supercapacitors. *ACS Appl. Mater. Interfaces* **2021**, *13*, 26870–26878. [CrossRef]
148. Luo, W.; Ma, Y.; Li, T.; Thabet, H.K.; Hou, C.; Ibrahim, M.M.; El-Bahy, S.M.; Xu, B.B.; Guo, Z. Overview of MXene/conducting polymer composites for supercapacitors. *J. Energy Storage* **2022**, *52*, 105008. [CrossRef]
149. Zhang, C.; Xu, S.; Cai, D.; Cao, J.; Wang, L.; Han, W. Planar supercapacitor with high areal capacitance based on Ti₃C₂/Polypyrrole composite film. *Electrochim. Acta* **2020**, *330*, 135277. [CrossRef]
150. Cao, S.; Zhao, T.; Li, Y.; Yang, L.; Ahmad, A.; Jiang, T.; Shu, Y.; Jing, Z.; Luo, H.; Lu, X.; et al. Fabrication of PANI@Ti₃C₂Tx/PVA hydrogel composite as flexible supercapacitor electrode with good electrochemical performance. *Ceram. Int.* **2022**, *48*, 15721–15728. [CrossRef]

151. Fu, J.; Yun, J.; Wu, S.; Li, L.; Yu, L.; Kim, K.H. Architecturally Robust Graphene-Encapsulated MXene Ti_2CTx @Polyaniline Composite for High-Performance Pouch-Type Asymmetric Supercapacitor. *ACS Appl. Mater. Interfaces* **2018**, *10*, 34212–34221. [CrossRef] [PubMed]
152. Ke, J.; Zhang, Y.; Wen, Z.; Huang, S.; Ye, M.; Tang, Y.; Liu, X.; Li, C.C. Designing strategies of advanced electrode materials for high-rate rechargeable batteries. *J. Mater. Chem. A* **2023**, *11*, 4428–4457. [CrossRef]
153. Kappler, J.; Klostermann, S.V.; Lange, P.L.; Dyballa, M.; Veith, L.; Schleid, T.; Weil, T.; Kästner, J.; Buchmeiser, M.R. Sulfur-Composites Derived from Poly(acrylonitrile) and Poly(vinylacetylene)—A Comparative Study on the Role of Pyridinic and Thioamidic Nitrogen. *Batter. Supercaps* **2023**, *6*, e202200522. [CrossRef]
154. Gupta, A.; Badam, R.; Matsumi, N. Heavy-Duty Performance from Silicon Anodes Using Poly(BIAN)/Poly(acrylic acid)-Based Self-Healing Composite Binder in Lithium-Ion Secondary Batteries. *ACS Appl. Energy Mater.* **2022**, *5*, 7977–7987. [CrossRef]
155. Karuppiah, C.; Besahhwured, S.L.; Wu, Y.-S.; Babulal, L.M.; Walle, K.Z.; Tran, H.K.; Wu, S.-H.; Jose, R.; Yang, C.-C. Patterning and a Composite Protective Layer Provide Modified Li Metal Anodes for Dendrite-Free High-Voltage Solid-State Lithium Batteries. *ACS Appl. Energy Mater.* **2021**, *4*, 11248–11257. [CrossRef]
156. Liang, B.; Liu, X.; Guo, X.; Zhao, J. Preparation and electrochemical properties of benzothiadiazole-benzotriazole donor-acceptor conductive polymer lithium-ion anode materials. *Synth. Met.* **2022**, *289*, 117112. [CrossRef]
157. Hu, J.; Jia, F.; Song, Y.-F. Engineering high-performance polyoxometalate/PANI/MWNTs nanocomposite anode materials for lithium ion batteries. *Chem. Eng. J.* **2017**, *326*, 273–280. [CrossRef]
158. Zhang, X.; Ji, W.; Xin, L.; Luedtke, A.; Qu, H.; Qiu, D.; Liu, M.; Zheng, D.; Qu, D. Effect of Carbon Additives on the Rate Performance of Redox Polymer Materials for Lithium Metal Batteries. *Ind. Eng. Chem. Res.* **2022**, *61*, 15989–15996. [CrossRef]
159. Wu, J.; Liu, S.; Huang, J.; Cui, Y.; Ma, P.; Wu, D.; Matyjaszewski, K. Fabrication of Advanced Hierarchical Porous Polymer Nanosheets and Their Application in Lithium-Sulfur Batteries. *Macromolecules* **2021**, *54*, 2992–2999. [CrossRef]
160. Chan, Y.-J.; Vedhanarayanan, B.; Ji, X.; Lin, T.-W. Doubling the cyclic stability of 3D hierarchically structured composites of 1T-MoS₂/polyaniline/graphene through the formation of LiF-rich solid electrolyte interphase. *Appl. Surf. Sci.* **2021**, *565*, 150582. [CrossRef]
161. Liu, T.; Kim, K.C.; Lee, B.; Chen, Z.; Noda, S.; Jang, S.S.; Lee, S.W. Self-polymerized dopamine as an organic cathode for Li- and Na-ion batteries. *Energy Environ. Sci.* **2017**, *10*, 205–215. [CrossRef]
162. Kim, J.-K.; Kim, Y.; Park, S.; Ko, H.; Kim, Y. Encapsulation of organic active materials in carbon nanotubes for application to high-electrochemical-performance sodium batteries. *Energy Environ. Sci.* **2016**, *9*, 1264–1269. [CrossRef]
163. Zhou, M.; Zhu, L.; Cao, Y.; Zhao, R.; Qian, J.; Ai, X.; Yang, H. Fe(CN)₆-4-doped polypyrrole: A high-capacity and high-rate cathode material for sodium-ion batteries. *RSC Adv.* **2012**, *2*, 5495–5498. [CrossRef]
164. Zhou, M.; Xiong, Y.; Cao, Y.; Ai, X.; Yang, H. Electroactive organic anion-doped polypyrrole as a low cost and renewable cathode for sodium-ion batteries. *J. Polym. Sci. Part B-Polym. Phys.* **2013**, *51*, 114–118. [CrossRef]
165. Liu, S.; Lei, T.; Song, Q.; Zhu, J.; Zhu, C. High Energy, Long Cycle, and Superior Low Temperature Performance Aqueous Na-Zn Hybrid Batteries Enabled by a Low-Cost and Protective Interphase Film-Forming Electrolyte. *ACS Appl. Mater. Interfaces* **2022**, *14*, 11425–11434. [CrossRef] [PubMed]
166. Su, Y.; Wang, X.; Zhou, S.; Sun, H.; Wang, B.; Liu, D.; Zhu, G. Porous rigid-flexible polymer membrane interface towards high-rate and stable zinc-ion battery. *J. Power Sources* **2023**, *560*, 232685. [CrossRef]
167. Xu, L.; Meng, T.; Zheng, X.; Li, T.; Brozena, A.H.; Mao, Y.; Zhang, Q.; Clifford, B.C.; Rao, J.; Hu, L. Nanocellulose-Carboxymethylcellulose Electrolyte for Stable, High-Rate Zinc-Ion Batteries. *Adv. Funct. Mater.* **2023**, *33*, 2302098. [CrossRef]
168. Wu, M.; Zhang, Y.; Xu, L.; Yang, C.; Hong, M.; Cui, M.; Clifford, B.C.; He, S.; Jing, S.; Yao, Y.; et al. A sustainable chitosan-zinc electrolyte for high-rate zinc-metal batteries. *Matter* **2022**, *5*, 3402–3416. [CrossRef]
169. Dong, Q.; Zhang, X.; Qian, J.; He, S.; Mao, Y.; Brozena, A.H.; Zhang, Y.; Pollard, T.P.; Borodin, O.A.; Wang, Y.; et al. A cellulose-derived supramolecule for fast ion transport. *Sci. Adv.* **2022**, *8*, eadd2031. [CrossRef]
170. Qiu, M.; Sun, P.; Cui, G.; Mai, W. Chaotropic Polymer Additive with Ion Transport Tunnel Enable Dendrite-Free Zinc Battery. *ACS Appl. Mater. Interfaces* **2022**, *14*, 40951–40958. [CrossRef]
171. Xie, X.; Fang, Z.; Yang, M.; Zhu, F.; Yu, D. Harvesting Air and Light Energy via “All-in-One” Polymer Cathodes for High-Capacity, Self-Chargeable, and Multimode-Switching Zinc Batteries. *Adv. Funct. Mater.* **2021**, *31*, 2007942. [CrossRef]
172. Liu, Y.; Xie, L.; Zhang, W.; Dai, Z.; Wei, W.; Luo, S.; Chen, X.; Chen, W.; Rao, F.; Wang, L.; et al. Conjugated System of PEDOT:PSS-Induced Self-Doped PANI for Flexible Zinc-Ion Batteries with Enhanced Capacity and Cyclability. *ACS Appl. Mater. Interfaces* **2019**, *11*, 30943–30952. [CrossRef] [PubMed]
173. Han, L.; Wang, L.; Chen, Z.; Kan, Y.; Hu, Y.; Zhang, H.; He, X. Incombustible Polymer Electrolyte Boosting Safety of Solid-State Lithium Batteries: A Review. *Adv. Funct. Mater.* **2023**, *33*, 2300892. [CrossRef]
174. Fan, L.-Z.; He, H.; Nan, C.-W. Tailoring inorganic–polymer composites for the mass production of solid-state batteries. *Nat. Rev. Mater.* **2021**, *6*, 1003–1019. [CrossRef]
175. Ma, C.; Cui, W.; Liu, X.; Ding, Y.; Wang, Y. In situ preparation of gel polymer electrolyte for lithium batteries: Progress and perspectives. *InfoMat* **2022**, *4*, e12232. [CrossRef]
176. Costa, C.M.; Lee, Y.-H.; Kim, J.-H.; Lee, S.-Y.; Lanceros-Méndez, S. Recent advances on separator membranes for lithium-ion battery applications: From porous membranes to solid electrolytes. *Energy Storage Mater.* **2019**, *22*, 346–375. [CrossRef]

177. Ward, I.M.; Hubbard, H.V.S.A.; Wellings, S.C.; Thompson, G.P.; Kaschmitter, J.; Wang, H. Separator-free rechargeable lithium ion cells produced by the extrusion lamination of polymer gel electrolytes. *J. Power Sources* **2006**, *162*, 818–822. [[CrossRef](#)]
178. Choi, J.; Zabihi, O.; Varley, R.J.; Fox, B.; Naebe, M. High Performance Carbon Fiber Structural Batteries Using Cellulose Nanocrystal Reinforced Polymer Electrolyte. *ACS Appl. Mater. Interfaces* **2022**, *14*, 45320–45332. [[CrossRef](#)]
179. Zhao, X.; Zhu, M.; Tang, C.; Quan, K.; Tong, Q.; Cao, H.; Jiang, J.; Yang, H.; Zhang, J. ZIF-8@MXene-reinforced flame-retardant and highly conductive polymer composite electrolyte for dendrite-free lithium metal batteries. *J. Colloid Interface Sci.* **2022**, *620*, 478–485. [[CrossRef](#)]
180. Chen, L.; Xue, P.; Liang, Q.; Liu, X.; Tang, J.; Li, J.; Liu, J.; Tang, M.; Wang, Z. A Single-Ion Polymer Composite Electrolyte via In Situ Polymerization of Electrolyte Monomers into a Porous MOF-Based Fibrous Membrane for Lithium Metal Batteries. *ACS Appl. Energy Mater.* **2022**, *5*, 3800–3809. [[CrossRef](#)]
181. Guan, J.; Feng, X.; Zeng, Q.; Li, Z.; Liu, Y.; Chen, A.; Wang, H.; Cui, W.; Liu, W.; Zhang, L. A New In Situ Prepared MOF-Natural Polymer Composite Electrolyte for Solid Lithium Metal Batteries with Superior High- Rate Capability and Long-Term Cycling Stability at Ultrahigh Current Density. *Adv. Sci.* **2023**, *10*, 2203916. [[CrossRef](#)] [[PubMed](#)]
182. Zhang, M.; Pan, P.; Cheng, Z.; Mao, J.; Jiang, L.; Ni, C.; Park, S.; Deng, K.; Hu, Y.; Fu, K.K. Flexible, Mechanically Robust, Solid-State Electrolyte Membrane with Conducting Oxide-Enhanced 3D Nanofiber Networks for Lithium Batteries. *Nano Lett.* **2021**, *21*, 7070–7078. [[CrossRef](#)] [[PubMed](#)]
183. Fergus, J.W. Ceramic and polymeric solid electrolytes for lithium-ion batteries. *J. Power Sources* **2010**, *195*, 4554–4569. [[CrossRef](#)]
184. He, K.; Chen, C.; Fan, R.; Liu, C.; Liao, C.; Xu, Y.; Tang, J.; Li, R.K.Y. Polyethylene oxide/garnet-type $\text{Li}_{6.4}\text{La}_3\text{Zr}_{1.4}\text{Nb}_{0.6}\text{O}_{12}$ composite electrolytes with improved electrochemical performance for solid state lithium rechargeable batteries. *Compos. Sci. Technol.* **2019**, *175*, 28–34. [[CrossRef](#)]
185. Sahore, R.; Armstrong, B.L.; Tang, X.; Liu, C.; Owensby, K.; Kalnaus, S.; Chen, X.C. Role of Scaffold Architecture and Excess Surface Polymer Layers in a 3D-Interconnected Ceramic/Polymer Composite Electrolyte. *Adv. Energy Mater.* **2023**, *13*, 2203663. [[CrossRef](#)]
186. Khomein, P.; Byeon, Y.-W.; Liu, D.; Yu, J.; Minor, A.M.; Kim, H.; Liu, G. Lithium Phosphorus Sulfide Chloride–Polymer Composite via the Solution–Precipitation Process for Improving Stability toward Dendrite Formation of Li-Ion Solid Electrolyte. *ACS Appl. Mater. Interfaces* **2023**, *15*, 11723–11730. [[CrossRef](#)]
187. Ren, Y.; Cui, Z.; Bhargav, A.; He, J.; Manthiram, A. A Self-Healable Sulfide/Polymer Composite Electrolyte for Long-Life, Low-Lithium-Excess Lithium-Metal Batteries. *Adv. Funct. Mater.* **2022**, *32*, 2106680. [[CrossRef](#)]
188. Ma, Q.; Zeng, X.-X.; Yue, J.; Yin, Y.-X.; Zuo, T.-T.; Liang, J.-Y.; Deng, Q.; Wu, X.-W.; Guo, Y.-G. Viscoelastic and Nonflammable Interface Design-Enabled Dendrite-Free and Safe Solid Lithium Metal Batteries. *Adv. Energy Mater.* **2019**, *9*, 1803854. [[CrossRef](#)]
189. Fan, X.; Ji, X.; Han, F.; Yue, J.; Chen, J.; Chen, L.; Deng, T.; Jiang, J.; Wang, C. Fluorinated solid electrolyte interphase enables highly reversible solid-state Li metal battery. *Sci. Adv.* **2018**, *4*, eaau9245. [[CrossRef](#)]

Disclaimer/Publisher’s Note: The statements, opinions and data contained in all publications are solely those of the individual author(s) and contributor(s) and not of MDPI and/or the editor(s). MDPI and/or the editor(s) disclaim responsibility for any injury to people or property resulting from any ideas, methods, instructions or products referred to in the content.